

Bridging the gap between numerics and experiment in free standing graphene

Maksim Ulybyshev^{1*}, Savvas Zafeiropoulos², Christopher Winterowd³, Fakher Assaad^{1,4}

¹Institute for Theoretical Physics, Julius-Maximilians-Universität Würzburg,
Am Hubland, D-97074 Würzburg, Germany

²Aix Marseille Univ, Université de Toulon, CNRS, CPT,
Marseille, France

³Johann Wolfgang Goethe-Universität Frankfurt am Main,
Frankfurt am Main, Germany

⁴ Würzburg-Dresden Cluster of Excellence ct.qmat
Am Hubland, 97074 Würzburg, Germany

*To whom correspondence should be addressed; E-mail: maksim.ulybyshev@physik.uni-wuerzburg.de.

We report results of large-scale quantum Monte Carlo (QMC) simulations of graphene. Using cutting-edge algorithmic improvements, we are able to consider spatial volumes, corresponding to 20808 electrons, that allow us to access energy scales of direct relevance to experiments. Using constrained random phase approximation (cRPA) estimates of short-ranged interactions combined with a Coulomb tail, we are able to successfully confront numerical and experimental estimates of the Fermi velocity renormalization. These results and their comparison with perturbation theory not only show the non-Fermi liquid character of graphene, but also prove the importance of lattice-scale physics and higher-order perturbative corrections beyond RPA for the quantitative description of the experimental data for the Fermi velocity renormalization in

suspended graphene.

Introduction

Since its experimental discovery in 2004 (1), graphene has attracted the attention of both the condensed-matter and the high-energy physics community. This is partly due to the fact that its low-energy electronic excitations can be described by a variant of quantum electrodynamics (QED) (2). As the electronic properties of graphene can be probed experimentally, it provides a unique opportunity to test the famous argument put forth by Dyson regarding the breakdown of the QED perturbative expansion (3). In conventional QED, the perturbative series in the fine-structure constant is asymptotic and gives increasingly accurate results up to a very large order, roughly the value of the inverse fine-structure constant (≈ 137). The action of the effective low-energy theory of graphene is written as $S = \int dt d^2x (i\bar{\psi}_a \gamma^0 \partial_0 \psi_a + i v_F \bar{\psi}_a \gamma^i \partial_i \psi_a - e \bar{\psi}_a \gamma^0 \psi_a A_0) + \frac{1}{2} \int dt d^3x (\partial_i A_0)^2$, where ψ_a is a two-flavour, four-component Dirac spinor. The effective fine-structure constant is rescaled by the ratio of the speed of light to the Fermi velocity v_F , which is roughly 300. It is thus thought that the perturbative series will display its asymptotic behavior at much lower orders than ordinary QED, demonstrating the inadequacy of perturbation theory. Ideally, the deviation between the perturbative results calculated within the low-energy continuum theory and experimental data should give a clear indication about the onset of this divergence (4).

Before one attempts such a comparison, one must be sure that suspended graphene, which features the unscreened electron-electron interaction, is described by the correct continuum field theory. This implies that other effects, such as the lattice scale physics or disorder, are either unimportant, or can be incorporated into the effective field theory (EFT) in a controlled way.

In the absence of a reliable continuum theory, the only way to proceed in a systematic manner is through non-perturbative numerical calculations of the many-body Hamiltonian. The in-

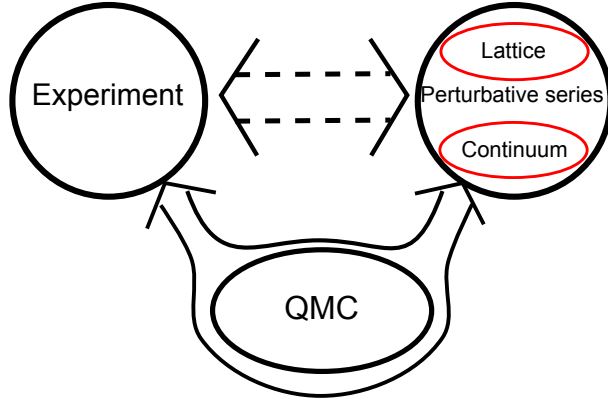


Figure 1: A schematic depiction of the relations between the different theoretical approaches which we are using to describe the electronic properties of free-standing graphene.

teracting tight-binding model on the hexagonal lattice is written as: $\hat{H} = -\kappa \sum_{\sigma, \langle x, y \rangle} (\hat{a}_{\sigma, x}^\dagger \hat{a}_{\sigma, y} + \text{h.c.}) + \frac{1}{2} \sum_{x, y} V_{x, y} \hat{q}_x \hat{q}_y$, where $\hat{a}_{\sigma, x}^\dagger$, $\sigma = \uparrow, \downarrow$ are creation operators for the electrons, \hat{q}_x is the electron charge operator, and $\kappa = 2.7$ eV is the nearest-neighbor hopping parameter (5). The next-nearest neighbor hopping matrix elements are neglected since they are an order of magnitude smaller. The matrix describing two-body interactions, $V_{x, y}$, provides a general description of the electron-electron coupling. As in the continuum, a perturbative series can be also formulated directly for this Hamiltonian, referred to as lattice perturbation theory (LPT), which is a systematic expansion for a given correlation function, organized in powers of V .

A schematic depiction of the relationships between the employed theoretical approaches is shown in Fig. 1: instead of a direct comparison of the continuum perturbative series with experiment, we establish a link between them through the help of QMC. First, we compare experimental data with the results of QMC calculations for the many-body Hamiltonian (thus verifying its validity). The QMC results are then compared with the perturbative calculations in both the continuum and lattice theory. The latter comparison reveals deficiencies in the EFT and demonstrates the importance of higher-order perturbative corrections.

We concentrate on the study of the Fermi velocity v_F . The renormalization of v_F in the

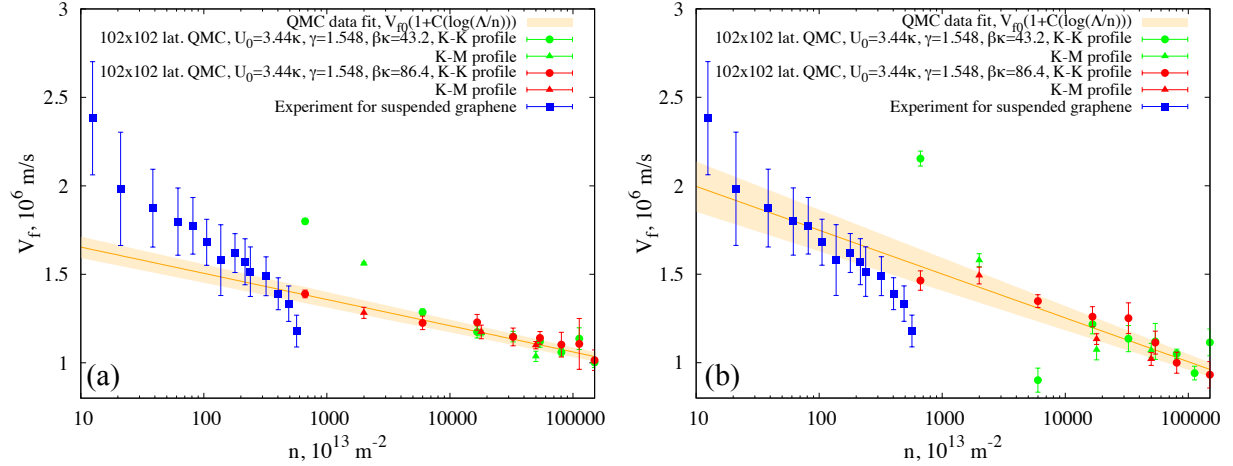


Figure 2: Comparison of experimental results for suspended graphene with QMC data obtained with potential variants I **(a)** and II **(b)**. The latter corresponds to suspended graphene, while the former has a reduced Coulomb tail. The Fermi velocity is computed via finite differences from the dispersion relation on the lattice. QMC results are computed for two values of temperatures, corresponding to inverse temperatures $\beta = 16eV^{-1}$ and $\beta = 32eV^{-1}$ or 43.2 and 86.4 in units of inverse hopping. For the high temperature results, the data point at the smallest density suffers from finite temperature artefacts (see discussion below), such that the two lowest density data points for the derivative are affected. We thus omit them in both K-K and K-M profiles when fitting QMC data with a logarithmic curve. The shaded area corresponds to the error of the logarithmic fit.

infrared limit has been already observed in several experiments (6, 7). Although a number of theoretical calculations have been performed using a perturbative approach (8, 9, 10, 4, 11), there is still no comprehensive comparison with fully non-perturbative calculations. Alternative methods based on various approximations were also used to compute the renormalization of v_F (12, 13). Here we solely comment on the validity of the perturbative approach.

Our goal hinges on the ability to carry out unbiased QMC simulations on lattices large enough so as to reach energy scales relevant for direct comparison to experiment. Fig. 2 shows that we can achieve this goal for the first time by using methods developed for lattice quantum chromodynamics, which broadly go under the name of hybrid Monte Carlo (HMC) and are perfectly suited to these types of calculations (14, 15, 16, 17). As one can see, one particular

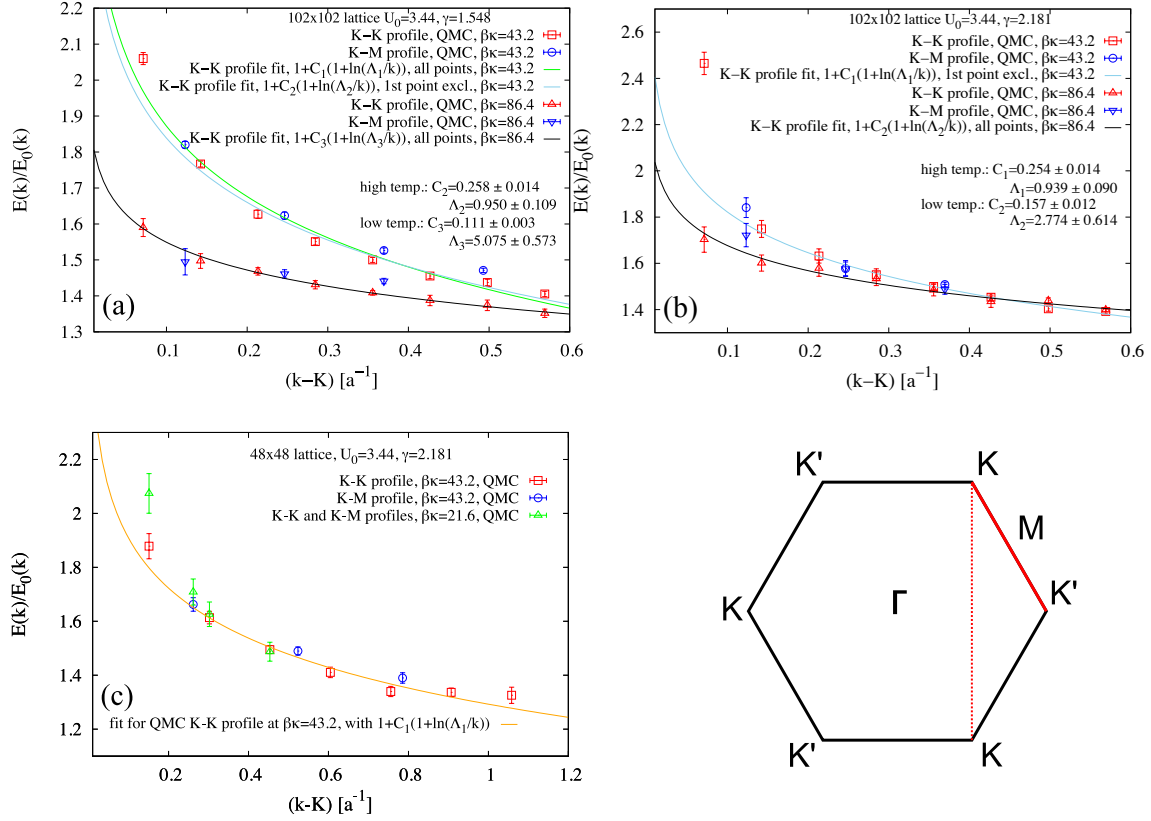


Figure 3: The renormalized dispersion of electrons at strong coupling using the electron-electron potential variant I (figure (a)) and the potential variant II ((b) and (c)). (a) and (b): QMC results on 102×102 lattice. (c) QMC results on 48×48 lattice. In all cases we fit the QMC data along the K-K line in the Brillouin zone (BZ) and the K-M profile is included for completeness. The horizontal axis is the distance from the Dirac point in units of inverse lattice step. The same units are used for the displayed values of the cutoff Λ .

interaction setup (Fig. 2b) shows remarkable agreement with the experiment in the limit of low densities, which corresponds to the low-energy limit of the dispersion relation.

Lattice Hamiltonian and experiment

We perform QMC calculations for the interacting tight-binding Hamiltonian cited above with the matrix of two-body interactions $V_{x,y}$ tuned in a way to model the electronic properties of suspended graphene. The salient features of $V_{x,y}$ are the on-site interaction $V_{x,x} = U_0$ and the

long-range Coulomb tail, $V_{x,y} = \gamma U_0 / (2|\vec{R}_{x,y}|)$, where $R_{x,y}$ is the distance between lattice sites in units of the spacing of the hexagonal lattice. In order to separately study both the effects of long-range and short-range interactions and to reproduce the experimental data for suspended graphene, we use three different interaction matrices $V_{x,y}$: variant I uses short-range couplings computed with the cRPA method in (18) and the strength of Coulomb tail is defined by the next-to-next-to-nearest coupling (15), thus $\gamma = 1.548$; variant II uses the same short-range couplings, but the long-range Coulomb tail is formed by a more complicated set of functions which fit the dielectric permittivity function $\varepsilon(k)$ (18), $\gamma = 2.181$ in this case; variant III is generally the same as variant I except for a shift of the nearest-neighbor (from 5.5 eV to 6.7 eV) and next-to-nearest-neighbor (from 4.1 eV to 4.5 eV) couplings. The details of potential variant II are explained in (19), and it should yield the closest match to experimental data. The difference between the results obtained with potential variants I and III is used to elucidate the role of the short-range couplings.

The QMC calculations were performed on 102×102 and 48×48 lattices at three different temperatures $T = 0.01157\kappa$, $T = 0.02315\kappa$ and $T = 0.04630\kappa$ in order to identify both finite-size and finite-temperature effects. Due to the fact that we are simulating a finite volume, the resolution in momentum is limited by the lattice size. Thus, the numerical differentiation needed for the computation of v_F brings about additional systematic errors (see supplementary material for examples). For this reason, we prefer to plot the renormalized dispersion relation $E(k)$ directly wherever possible. Indeed, the logarithmic renormalization of the Fermi velocity, $v_F(k) = v_{F,0}(1 + C \ln \Lambda/k)$, also leads to the logarithmic renormalization of the energy itself: $E(k) = E_0(k)[1 + C(1 + \ln \Lambda/k)]$, where $E_0(k)$ is the free dispersion relation. Thus we have a well-defined fitting function for the QMC and LPT data sets.

The renormalized dispersion relation for potential variants I and II is shown in Fig. 3. Unlike previous QMC studies (20), the lattice size appears to be large enough to clearly observe

the non-linear dispersion relation. First we look at the results on a 102×102 lattice for both smaller (Fig. 3a) and larger (Fig. 3b) Coulomb tails. The results at intermediate temperature $T = 0.02315\kappa$, which corresponds to inverse temperature $\beta = 43.2/\kappa$ show sizeable finite-temperature effects: while all points except the first one are aligned along the logarithmic curve, the points at the lowest momenta are shifted upwards for both a large and small Coulomb tail. This feature of the data cannot be attributed to finite-size effects: it is the most pronounced at lower energies such that lower temperatures should lead to the enhancement of this effect. We however observe the opposite behaviour: the low-temperature data for the 102×102 lattice is perfectly aligned according to the logarithmic fit for both sets of potentials.

A similar effect can be also observed on the 48×48 lattice if we compare the two large temperatures: $T = 0.02315\kappa$ and $T = 0.04630\kappa$ (Fig. 3c). Once we reduce both the inverse temperature and the lattice size by a factor of two, we observe a similar enhancement of the first data point with respect to the logarithmic curve, in comparison to the same lattice at a lower temperature. Notably, further points do not experience significant finite-temperature effects in perfect agreement with the 102×102 lattice data at momentum $|k - K| > 0.3a^{-1}$. Hence, we conclude that these finite-temperature effects, that drive the dispersion relation (hence also v_F) upwards with respect to the logarithmic curve, should be observed in experiments.

A comparison with experiment is shown in Fig. 2, where the QMC data is displayed alongside the experimental data from (6). The renormalized Fermi velocity is plotted as a function of density n , for two variants of the two-body interaction potential and two lower temperatures. As suggested by the previous analysis of the temperature effects, the first point in the dispersion relation obtained at higher temperature should be disregarded, which in turn affects the two first points for v_F . On the contrary, the lower temperature data can be used down to the lowest density where the experimental curve starts.

In agreement with the analysis of the $E(k)$ curves, the first points of the higher temperature

data sets show substantial deviations from the logarithmic curve, while the points at higher densities are indistinguishable for both higher and lower temperatures.

The logarithmic fitting of the QMC data with its error bars displayed in Fig. 2a shows that the Coulomb tail corresponding to $\gamma = 1.548$ is too small to reproduce the experimental data. This is understandable, as the Coulomb tail is reduced here in comparison with that in suspended graphene. In contrast, the logarithmic fit of QMC data for the larger Coulomb tail (Fig. 2b) demonstrates a remarkably good agreement with the experimental data points in the limit of small densities. It would be interesting to investigate the origin of the drop of the experimental points below the logarithmic curve which appear at roughly $n = 2 \times 10^{15} m^{-2}$. There is one peculiarity of the experimental setup which could potentially play a role here: the actual measurements are done at a finite gate voltage, which is equivalent to the introduction of a chemical potential. This is certainly a physically different situation from the one simulated in QMC, and, as suggested in (4, 12), the finite density of charge carriers can impose additional screening on the Coulomb interaction. In the limit of small densities this effect disappears, and thus we observe better agreement between experiment and QMC.

Another observation is that the extrapolated QMC data and experiment agree not only in terms of the coefficient in front of the logarithm (inclination of the curve in the figure 2), but also in the vertical shift. As we will show later, this shift is determined by the ultraviolet cutoff, which is strongly dependent on the short-range part of the electron-electron interaction. This means that the cRPA potentials, taken from (18) are suitable for graphene: the tight-binding Hamiltonian with the matrix of interaction defined by potentials variant II (PII) is indeed a reliable model to describe the electronic properties of graphene even in the strongly-correlated regime.

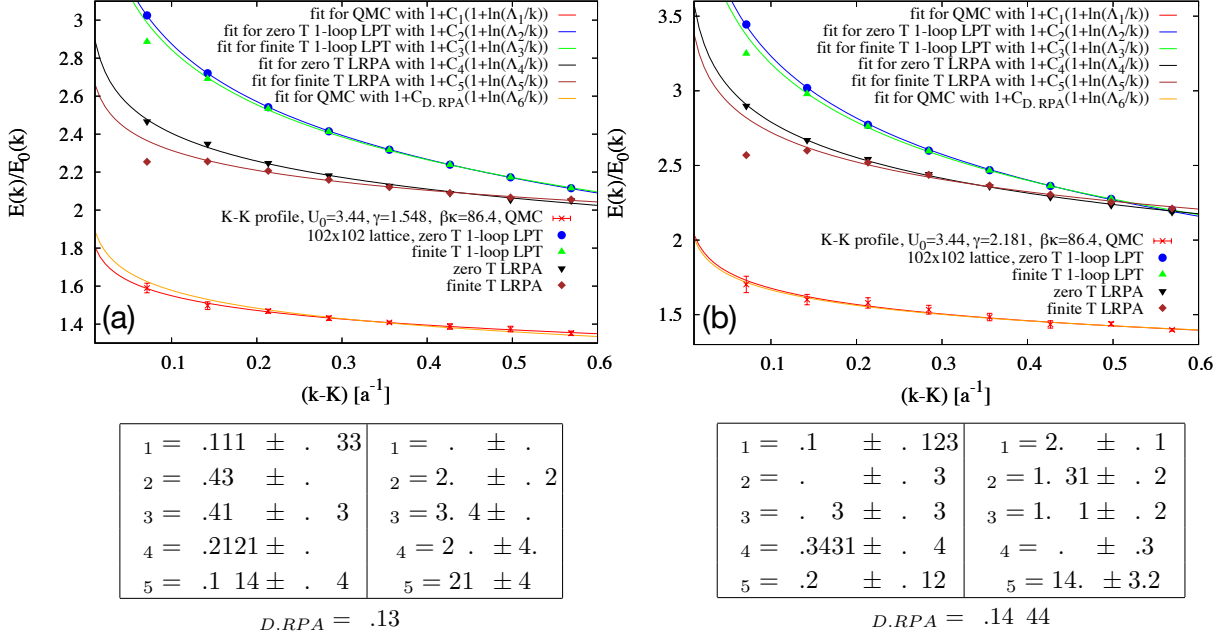


Figure 4: Comparison of QMC data with perturbative results on the lattice (zero temperature and finite-temperature one-loop LPT, also zero temperature and finite-temperature lattice random phase approximation (LRPA)) as well as in the continuum. The zero-temperature RPA is used in the latter case. The potential PI is shown on the left (a) and the variant PII is shown on the right (b). Both LPT and QMC results are obtained on a 102×102 lattice and we consider the K-K profile in the BZ. The fitting parameters C_i and Λ_i are shown in the tables below the corresponding figures. Cutoff values are expressed in units of inverse lattice spacing. The momentum closest to the Dirac point is omitted in the fit of the finite-temperature LPT data, as previously mentioned.

Lattice Hamiltonian and perturbative series

As the tight-binding Hamiltonian provides good agreement with experiment, one can comment on the accuracy of the perturbative series by comparing its results to the QMC data. This approach is more precise (see e.g. figure 2a) and is also more flexible, as one can simply vary the parameters in the QMC simulations.

The comparison of LPT, effective field theory (EFT) and QMC data is shown in Fig. 4 again for potentials PI and PII. The LPT results also include finite-temperature profiles, both

for one-loop and RPA self-energy corrections. The description of both continuum and lattice perturbation theory can be found in the supplementary material.

By examining the values of the coefficients C in front of the logarithm, we conclude that no perturbative approach can satisfactorily describe the QMC data. The continuum RPA gets closest to QMC data but this can be attributed to the fact that the cutoff is a free parameter. This is unlike the case of LPT, where we do not have any additional free parameters which can be adjusted to obtain better agreement with QMC. The coefficient C from continuum RPA is close to the one extracted from QMC data produced with a stronger Coulomb tail (see Fig. 4b). However, we argue that it is merely a random coincidence, since the agreement becomes much worse for the data produced with a weaker Coulomb tail. This data is displayed in Fig. 4a, where the difference between the respective C coefficients grows to $\approx 20\%$. Moreover, LPT data should in principle compare better to QMC profiles, since LPT takes into account lattice-scale phenomena, including the cRPA interaction potentials. However, we find that this is not the case, since the C coefficients extracted from the LPT profiles are even further away from the QMC data than those computed within the continuum EFT.

A more detailed comparison between LPT and QMC datasets also reveals a clear qualitative difference: finite-temperature effects are driving the LPT profile down with respect to the logarithmic curve at small momenta, while the QMC data shows the exact opposite trend. This is clear if one compares e.g. LRPA data from Fig. 4b with the low momentum behaviour of two QMC data profiles at different temperatures from Fig. 3b. One can thus conclude that the comparison of LPT and QMC data unambiguously shows the importance of higher-order corrections in a quantitative description of the renormalization of the Fermi velocity in graphene. This effect can be potentially confirmed experimentally providing the measurements are done in suitable intervals of temperatures and densities. In particular, for a better perturbative description the inclusion of vertex corrections should also be considered. These have been shown

to play an important role in Schwinger-Dyson (SD) studies (21). In order to accurately describe the dynamical mass generation as well as the Fermi velocity renormalization in the SD framework, one is forced to include a gauge invariant form of the vertex whose longitudinal part is determined by the Ward identity and whose transverse part is free of kinematic singularities (22). This, along with the inclusion of dynamic screening from the Lindhard function has been shown to give good results.

Next we turn to the discrepancy between EFT curves and LPT/QMC data. Since the Feynman diagrams included in LPT and EFT data are essentially the same, there are two possible sources for this discrepancy: first, the influence of lattice-scale physics, most notably, the presence of a physical cutoff accompanied by the curvature of the electronic dispersion away from the Dirac points; second, the differences between lattice potentials and continuous Coulomb interaction at intermediate distances.

Since LPT takes into account the latter effect, we can try to isolate the reasons for the discrepancies between the EFT and LPT data through a comparison with LPT at different orders of perturbation theory. One-loop LPT yields an almost identical C as the one-loop EFT: compare $C = 0.5986 \pm 0.0039$ in LPT for potential variant II and $C = 0.626$ in EFT for Coulomb potential with the same long-range tail (see Fig. 4b). This demonstrates that modifications to the cRPA potentials at intermediate distances do not influence the value of C substantially. In contrast to the one-loop approximation, a comparison of the C coefficients extracted from LPT and the ones from EFT at the RPA level shows substantial differences. This suggests that lattice-scale physics is important. The origins of this discrepancy are explained in detail in the next section.

We now comment on the influence of short-range couplings (see Fig. 5). We compare potential variant I and potential variant III, which differ mostly in the nearest-neighbor coupling. If we look at the LPT data, the effect is clearly confined to the change of the cutoff, with the

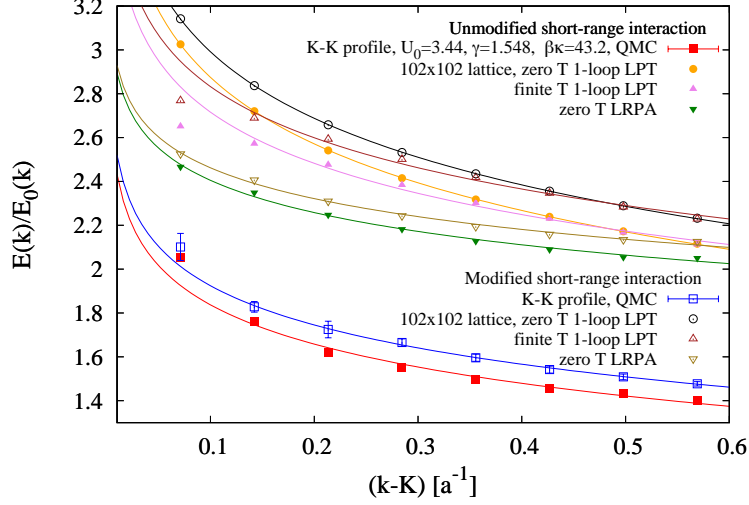


Figure 5: The role of the short-range couplings in determining the renormalized dispersion relation. We compare potentials PI and PIII, which differ only in the interaction between nearest-neighbors and next-to-nearest neighbors. The logarithmic fits are shown for all QMC and LPT data sets (the first points are omitted in the fits for finite-temperature profiles). The results of fitting the QMC data: C coefficients for potentials PI and PIII respectively are equal to $C_I = 0.258 \pm 0.014$ and $C_{III} = 0.258 \pm 0.006$; cutoff values for the same curves are equal to $\Lambda_I = 0.950 \pm 0.109$ and $\Lambda_{III} = 1.318 \pm 0.06$.

coefficient in front of the logarithm remaining constant. As a result, the dispersion curves are uniformly shifted vertically with respect to each other. The effect is exactly the same for QMC data, since the C coefficients for two curves are almost identical (see the caption to the Fig. 5). This result is consistent with the general renormalization group (RG) point of view on the role of the couplings at different length scales. The short-range interactions in graphene are irrelevant at the infrared fixed point, and thus they can not change the qualitative behaviour of v_F at low momentum. However, they can still influence the results at a quantitative level by changing the parameters which are not fixed by the RG flow, such as the cutoff. Furthermore, these results show that fixing the cutoff is not a trivial procedure, as it is not solely defined by

the bandwidth, but depends on interactions which are irrelevant in the RG sense.

Lattice vs continuum perturbative series

In order to present a more clear comparison of EFT and LPT, we eliminate the cRPA modification to the Coulomb interaction and employ a two-body interaction, $V_{x,y}$, where all elements except the on-site one are defined by the Coulomb tail. Here we take $\gamma = 1.548$, which corresponds to an effective fine structure constant of $\alpha = 1.778$.

A comparison between LPT and continuum EFT at the one-loop and RPA level is shown in Fig. 6. We again observe that LPT and the continuum theory start to deviate at the RPA level since it is impossible to describe the lattice data using C taken from the continuum RPA expression and leaving only Λ as a free parameter. One recalls that the polarization bubble is only naively divergent in $(2 + 1)$ -QED and can be computed using one of the conventional continuum regularization schemes to take care of the ultraviolet divergences, and thus there are no additional free parameters that can be added.

To further investigate this deviation between the continuum and lattice RPA calculations, we consider the dimensionless quantity $\mathcal{P} = \Pi^{(0)}P$, where P is the polarization and $\Pi^{(0)}$ is the free Coulomb propagator. On the lattice, it corresponds to $\mathcal{P} = \text{Tr}(\Pi^{(0)}P)$, where the trace is taken over the sublattice index. This quantity, which depends on both frequency and momentum, is shown in figures 6b and 6c. Clearly, there are substantial differences between the lattice and continuum expressions. A detailed analysis is presented in the supplementary material, while here we simply state the result that these differences can be attributed to two distinct effects: a constant shift of \mathcal{P} at the Γ point is due to inter-valley scattering and a linear correction to \mathcal{P} around the Γ point due to the finite cutoff.

Both of these effects can be included in the continuum EFT, but at a large cost. Inter-valley scattering can be described by the modified expression for the charged current in the EFT:

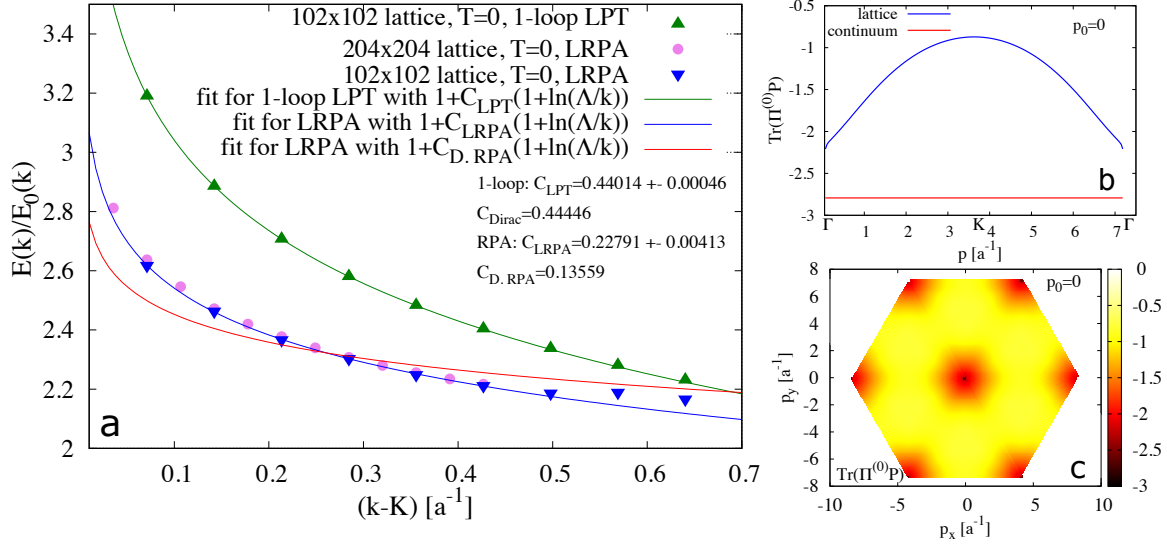


Figure 6: **(a)** A comparison of lattice and continuum perturbation theory in the strongly-coupled regime. The on-site interaction is $U_0 = 3.42\kappa$, all other potentials are defined by the Coulomb tail with $\gamma = 1.548$. For reference, we also include the values of the C coefficients in one-loop and RPA continuum Dirac theory. **(b)** A comparison of $\text{Tr}(\Pi^{(0)}P)$ computed in LPT and in the continuum. The external frequency is set to zero and the external momentum runs along the ΓK line. **(c)** A depiction of $\text{Tr}(\Pi^{(0)}P)$ computed in LPT within the BZ on a 102×102 lattice at zero frequency.

$\tilde{j}_0 = \bar{\psi}_a \gamma_0 (I + \sum_j \exp(-i\vec{x}\Delta\vec{\mathcal{K}}_j\tau_3/2)\tau_1 \exp(i\vec{x}\Delta\vec{\mathcal{K}}_j\tau_3/2))\psi_a$, where τ_j are Pauli matrices in valley space and $\Delta\vec{\mathcal{K}}_j$, $j = 1, 2, 3$ are lattice vectors connecting a single Dirac point with the three neighboring non-equivalent Dirac points. This modified vertex should be accompanied by the addition of higher-dimensional kinetic terms to the QED Lagrangian in order to reproduce the non-linear dispersion relation away from the Dirac points. Moreover, we should employ a hard cutoff procedure in all loop integrals. An example of such a calculation for the polarization can be found in the supplementary material and we indeed get a term $\sim |\vec{p}|/\Lambda$ in \mathcal{P} . Interestingly, it is possible to show that both inter-valley scattering and the hard UV cutoff induce much smaller corrections in the one-loop electron self-energy, which is consistent with our observation that the discrepancies between LPT and the EFT appear only at the level of RPA. Further details regarding procedures for modifying the continuum EFT are discussed in detail in the

supplementary material.

Conclusions and Outlook

We have explicitly demonstrated the logarithmic divergence of the Fermi velocity in graphene in the vicinity of the Dirac point using non-perturbative QMC calculations. In agreement with RG arguments, the long-range Coulomb tail defines the coefficient in front of the logarithm, while short-range interactions are responsible for non-universal features such as the value of cutoff Λ in the logarithm.

The logarithmic fit of QMC data for potential PII shows excellent agreement with the experiment, which signals that the interacting tight-binding model with the potentials described in (18) and (19) can serve as a reliable model for suspended graphene.

It is clear that the underlying lattice structure plays a large role in suspended graphene. It becomes apparent first in the polarization bubble, and it suggests that the lattice effects play an even greater role in multi-loop calculations and that continuum QED is unable to describe LPT or QMC data at a quantitative level in the strongly-coupled regime. Thus, LPT should replace continuum EFT if one wants to achieve agreement with experimental and non-perturbative QMC data. Also, it is more convenient to use LPT in the analysis of the convergence of the perturbative series, as it enables a direct comparison with QMC.

A detailed comparison of LPT and QMC data shows that the standard RPA is not enough to describe the QMC results. From the theoretical side, one should possibly include vertex corrections or even go for higher-order diagrams. It might even be a signal of a general breakdown of the perturbative expansion. In order to definitively identify the breakdown, LPT should be considered at higher orders and compared with the existing QMC data. From an experimental point of view, the clearest way to demonstrate this effect is to estimate the temperature corrections. If one measures v_F in the “high-temperature limit” at momenta corresponding to the

energy in the free dispersion relation $E_0(k) \leq 2...3T$, then the deviations of the Fermi velocity upwards from the logarithmic curve can be regarded as a qualitative sign of higher-order perturbative corrections beyond RPA. Potentially, such a measurement combined with higher-order LPT calculations can demonstrate the onset of the divergence of the asymptotic series of strongly-correlated QED.

Acknowledgments

This work mainly benefited from access to the Irène Joliot-Curie supercomputer of the Très grand centre de calcul (TGCC) of the Commissariat à l'énergie atomique et aux énergies alternatives (CEA) in France as part of a “grand challenge” project (project id: gch413) awarded by GENCI (Grand Equipement National de Calcul Intensif) as well as through project gen2271. It also benefited from access to the Jean Zay supercomputer at the Institute for Development and Resources in Intensive Scientific Computing (IDRIS) in Orsay, France and from access to the Occigen supercomputer under projects A0080511504 and A0080502271, hosted by the Centre Informatique National de l'Enseignement Supérieur (CINES) at Montpellier, France. It was also partially supported by the HPC Center of Champagne-Ardenne ROMEO and by the GPU cluster of the Institute of Theoretical Physics of the University of Heidelberg. Additional resources were provided by the Gauss Centre for Supercomputing e.V. (www.gauss-centre.eu) through the John von Neumann Institute for Computing (NIC) on the GCS Supercomputer JUWELS (23) at Jülich Supercomputing Centre (JSC). FFA acknowledge financial support from the DFG through the Würzburg-Dresden Cluster of Excellence on Complexity and Topology in Quantum Matter - ct.qmat (EXC 2147, project-id 39085490), through the SFB 1170 ToCoTronics. MU thanks the DFG for financial support under the projects UL444/2-1. CW acknowledges support by the Deutsche Forschungsgemeinschaft (DFG, German Research Foundation) through the CRC-TR 211 'Strong-interaction matter under extreme conditions'–

project number 315477589 – TRR 211. The authors would like to thank Eugene Mishchenko for insightful discussions regarding the perturbative calculations. FFA and MU would like to thank Shaffique Adam for discussions during initial stages of this project. FFA would like to thank H.K. Tang, J. N. Leaw, J. N. B. Rodrigues, I. F. Herbut, P. Sengupta and S. Adam for previous collaborations on the subject. We also thank T. Stauber for providing the access to experimental data.

References

1. K. S. Novoselov, *et al.*, *Science* **306**, 666 (2004).
2. V. N. Kotov, B. Uchoa, V. M. Pereira, F. Guinea, A. H. Castro Neto, *Rev. Mod. Phys.* **84**, 1067 (2012).
3. F. J. Dyson, *Phys. Rev.* **85**, 631 (1952).
4. E. Barnes, E. H. Hwang, R. E. Throckmorton, S. Das Sarma, *Phys. Rev. B* **89**, 235431 (2014).
5. N. M. R. Peres, *Rev. Mod. Phys.* **82**, 2673 (2010).
6. D. Elias, *et al.*, *Nature Physics* **7**, 701 (2011).
7. G. L. Yu, *et al.*, *Proceedings of the National Academy of Sciences* **110**, 3282 (2013).
8. J. González, F. Guinea, M. A. H. Vozmediano, *Phys. Rev. B* **59**, R2474 (1999).
9. D. T. Son, *Phys. Rev. B* **75**, 235423 (2007).
10. I. S. Tupitsyn, N. V. Prokof'ev, *Phys. Rev. Lett.* **118**, 026403 (2017).
11. E. G. Mishchenko, *Phys. Rev. Lett.* **98**, 216801 (2007).

12. T. Stauber, *et al.*, *Phys. Rev. Lett.* **118**, 266801 (2017).
13. A. Sharma, P. Kopietz, *Phys. Rev. B* **93**, 235425 (2016).
14. J. E. Drut, T. A. Lähde, *Phys. Rev. Lett.* **102**, 026802 (2009).
15. M. V. Ulybyshev, P. V. Buividovich, M. I. Katsnelson, M. I. Polikarpov, *Phys. Rev. Lett.* **111**, 056801 (2013).
16. J. E. Drut, T. A. Lähde, *arXiv e-prints* p. arXiv:1304.1711 (2013).
17. W. Armour, S. Hands, C. Strouthos, *Phys. Rev. B* **84**, 075123 (2011).
18. T. O. Wehling, *et al.*, *Phys. Rev. Lett.* **106**, 236805 (2011).
19. D. Smith, L. von Smekal, *Phys. Rev. B* **89**, 195429 (2014).
20. H.-K. Tang, *et al.*, *Science* **361**, 570 (2018).
21. M. E. Carrington, C. S. Fischer, L. von Smekal, M. H. Thoma, *Phys. Rev. B* **94**, 125102 (2016).
22. J. S. Ball, T.-W. Chiu, *Phys. Rev. D* **22**, 2542 (1980).
23. Jülich Supercomputing Centre, *Journal of large-scale research facilities* **5** (2019).

Supplementary materials

Supplementary Text

Figs. S1 to S15

References (1-25)

Supplementary material for: Bridging the gap between numerics and experiment in free standing graphene

Maksim Ulybyshev^{1*}, Savvas Zafeiropoulos², Christopher Winterowd³,
Fakher Assaad^{1,4}

¹Institute for Theoretical Physics, Julius-Maximilians-Universität Würzburg,
Am Hubland, D-97074 Würzburg, Germany

²Aix Marseille Univ, Université de Toulon, CNRS, CPT,
Marseille, France,

³Johann Wolfgang Goethe-Universität Frankfurt am Main,
Frankfurt am Main, Germany

⁴ Würzburg-Dresden Cluster of Excellence ct.qmat
Am Hubland, 97074 Würzburg, Germany

*To whom correspondence should be addressed; E-mail: maksim.ulybyshev@physik.uni-wuerzburg.de

1 Numerical setup

In this section we briefly describe our lattice quantum Monte Carlo (QMC) setup and the calculation of the relevant observables. For a more detailed discussion we refer the reader to [\(1, 2, 3\)](#). The goal of hybrid Monte Carlo is to efficiently and faithfully sample the functional integral representation of the partition function, $Z = \text{Tr} e^{-\beta\hat{\mathcal{H}}}$. The trace is performed using fermionic coherent states by first breaking up the continuous Euclidean time interval, $[0, \beta)$, into N_τ slices. In order to compute matrix elements of the two-body interaction term, $\hat{\mathcal{H}}_{\text{int}}$, we must introduce a scalar bosonic field, ϕ , on each time-slice and lattice site. This is done through the Hubbard-

Stratonovich transformation

$$e^{\delta\tau \sum_{x,y} V_{x,y} \hat{q}_x \hat{q}_y} \cong \int \mathcal{D}\phi e^{-\frac{1}{2\delta\tau} \sum_{x,y} \phi_x V_{x,y}^{-1} \phi_y} e^{i \sum_x \phi_x \hat{q}_x}, \quad (1)$$

where the interaction is now bilinear in the fermion operators through the charge operator $\hat{q}_x \equiv \hat{a}_{x,\uparrow}^\dagger \hat{a}_{x,\uparrow} + \hat{a}_{x,\downarrow}^\dagger \hat{a}_{x,\downarrow} - 1$. In the current paper, we have adopted a more complicated version of the Hubbard-Stratonovich decomposition, which introduces two separate scalar fields which couple to spin and charge density respectively. This is done by using the following identity for the on-site term

$$\frac{V_{x,x}}{2} \hat{q}_x^2 = \frac{\eta V_{x,x}}{2} \hat{q}_x^2 - \frac{(1-\eta)V_{x,x}}{2} \hat{s}_x^2 + (1-\eta)V_{x,x} \hat{s}_x, \quad (2)$$

where $\hat{s}_x \equiv \hat{a}_{x,\uparrow}^\dagger \hat{a}_{x,\uparrow} - \hat{a}_{x,\downarrow}^\dagger \hat{a}_{x,\downarrow}$ is the spin operator and $\eta \in [0, 1]$ is a free parameter. Further details regarding the application of this technique to the case of the long-range Coulomb tail can be found in (4). This is done in order to avoid possible ergodicity issues in the sampling of the functional integral. This procedure is extensively discussed in (5), which we refer to for further details.

In the functional integral formulation, the thermal expectation values of observables are computed in the usual way,

$$\langle \mathcal{O} \rangle = \frac{1}{Z} \int \mathcal{D}\phi \det M[\phi]^2 \mathcal{O} e^{-S_B[\phi]}, \quad (3)$$

where M is the bilinear fermion operator and S_B is the quadratic bosonic action that results from applying (1) at each time slice. After carrying out a particle-hole transformation one can show that the action, for each Hubbard-Stratonovich field, is invariant under time-reversal symmetry. This symmetry leads to the absence of negative sign problem (6), and one will show that the fermion determinant in the above equation is real. To evaluate the expectation value one can adopt the Blankenbecler, Scalapino, Sugar (BSS) algorithm (7) and work with the determinant directly. Such an approach invariably leads to a computational time that scales as $N_\tau N^3$ for a

single sweep (8, 9). Here, N corresponds to the number of spatial sites in a single Euclidean time-slice.

There exists an alternative technique for this procedure, namely, hybrid Monte Carlo (10) (HMC). This algorithm is typically used in lattice quantum chromodynamics (LQCD) calculations, but can be adapted to condensed-matter systems. One can evaluate the determinant stochastically,

$$\det M[\phi]^2 \propto \int \mathcal{D} \{ \eta, \eta^\dagger \} e^{-\eta^\dagger (M[\phi]M^\dagger[\phi])^{-1} \eta} \quad (4)$$

and sample both over the Hubbard-Stratonovich and pseudo-fermion fields. In principle, we add more statistical fluctuations to the system, thus increasing the prefactor in the scaling of the algorithm with the system size. However, when the fermion matrix is not too ill-conditioned, HMC becomes very appealing and outperforms the BSS approach. This turns out to be the case here, where the scaling of the computational time with volume and number of time slices is $(NN_\tau)^{1.5}$, thus larger prefactor is compensated by better scaling for large systems.

In the QMC calculations performed for this study, we have only slightly modified the algorithm used in the previous functional integral studies of graphene (e.g. in (11)) by employing a different symplectic integrator in the molecular dynamics (12).

The renormalized dispersion of the quasiparticles is obtained through the fermion propagator, which is defined as

$$G(x, \tau) = \frac{\text{Tr} \{ \hat{a}_x e^{-\tau \hat{\mathcal{H}}} \hat{a}_0^\dagger e^{-(\beta-\tau) \hat{\mathcal{H}}} \}}{Z}, \quad (5)$$

where the operators appearing in the numerator are in the Heisenberg representation and we have assumed translational invariance in both space and in Euclidean time. In our functional integral setup, (5) can be recast in terms of elements of the inverse fermion operator

$$G(\vec{k}, \tau) = \sum_x e^{-i\vec{k} \cdot \vec{x}} \langle M_{x,\tau;0,0}^{-1} \rangle, \quad (6)$$

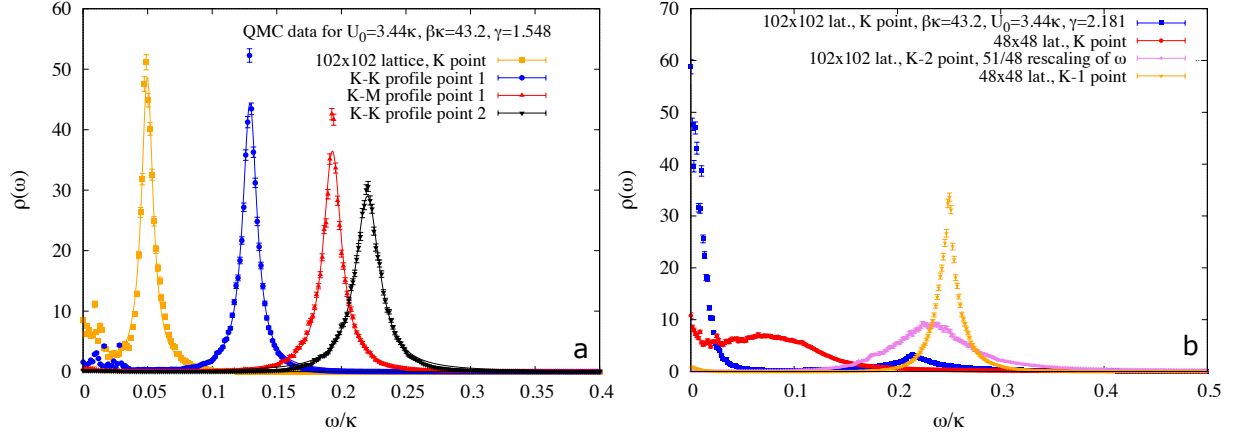


Figure S1: **(a)** Several spectral functions, reconstructed with the help of stochastic MEM at various points in the BZ. The data are shown for potential variant I with no additional rescaling in order to reside firmly within the strongly-coupled regime. We display the spectral functions for the K point and the three other points closest to it. The resonances are fitted with a Lorentzian ansatz, $Z/((\omega - \omega_0)^2 + \Gamma^2)$. We note that a gap appears at the Dirac point. This is indicated by the presence of a large peak in the spectral function at the Dirac point which is shifted from the origin, with a smaller peak existing at zero frequency. **(b)** Spectral functions at the Dirac point and in its vicinity. We compare the results obtained on the 102×102 lattice (at the Dirac point and at the second point in momentum along the K-K line in the BZ) with those for the 48×48 lattice (again at the Dirac point and at the first point in K-K profile). The data shown in the plots were produced with potential variant II (see main text for definition). A comparison of the 102×102 lattice data with the spectral function in figure (a) at the K point shows that the gap disappears with an increased Coulomb tail, which drives us away from the antiferromagnetic phase transition (see (9)). Moreover, the comparison of the spectral functions at the K point, computed on the 48×48 and 102×102 lattices, shows that the gap we sometimes see is merely a finite-volume artifact. The double-peak structure seen at smaller lattice sizes disappears as the number of sites is increased.

where the expectation value is taken as in (3), and we have projected to a momentum k residing within the BZ. In practice, $G(\vec{k}, \tau)$ is 2×2 matrix in sublattice space and we are using its trace for further processing. In order to express this quantity in terms of the eigenvalues of the many-body Hamiltonian, we introduce the well-known spectral representation of the propagator

$$G(\vec{k}, \omega) = \int_{-\infty}^{+\infty} \frac{d\omega'}{2\pi} \frac{\rho(\vec{k}, \omega')}{-i\omega + \omega'}, \quad (7)$$

where we have also introduced the density of states, which is given as

$$\rho(\vec{k}, \omega) = \frac{2\pi}{Z} \sum_{n,m} \delta(E_m - E_n - \omega) |\langle m | \hat{a}_k^\dagger | n \rangle|^2 (e^{-\beta E_n} + e^{-\beta E_m}). \quad (8)$$

Here E_n and E_m refer to eigenvalues of the Hamiltonian whose corresponding states have total momentum which differ by k . This analysis is completely generic, and for any Euclidean correlation function there will exist a corresponding spectral function. On the lattice, we compute observables in the Euclidean time representation, and thus one can transform (7) to obtain the Green-Kubo relation

$$G(\vec{k}, \tau) = \frac{1}{\pi} \int_0^{+\infty} d\omega K(\omega, \tau) \rho(\vec{k}, \omega), \quad (9)$$

where the kernel is given by $K(\omega, \tau) = \cosh[\omega(\tau - \beta/2)] / \cosh[\omega\beta/2]$. Obtaining the density of states through the inversion of (9) is an ill-defined problem, as one is attempting to reconstruct an analytic function of frequency from N_τ data points and their associated statistical errors. The inverse problem can be dealt with by applying the stochastic maximum entropy method (MEM) (13). In this work, we have used the publicly available algorithms for lattice fermions (ALF) code, which contains an implementation of the stochastic MEM (14, 15). In Fig. (S1), one can see some of the results of this spectral reconstruction. Using the reconstructed spectral function, one can obtain estimate for the energy of the quasiparticle excitations $\omega_0(\vec{k})$ by finding the peak of the spectral function. The cost of performing the inverse problem is that one must have data with very small statistical errors.

2 Justification of QMC

In order to prove the correctness of the numerical procedures, we check that at small interaction the QMC results converge towards lattice perturbation theory. In order to do so, we take the potential variant II (see the main text for details) and uniformly rescale it so that the on-site

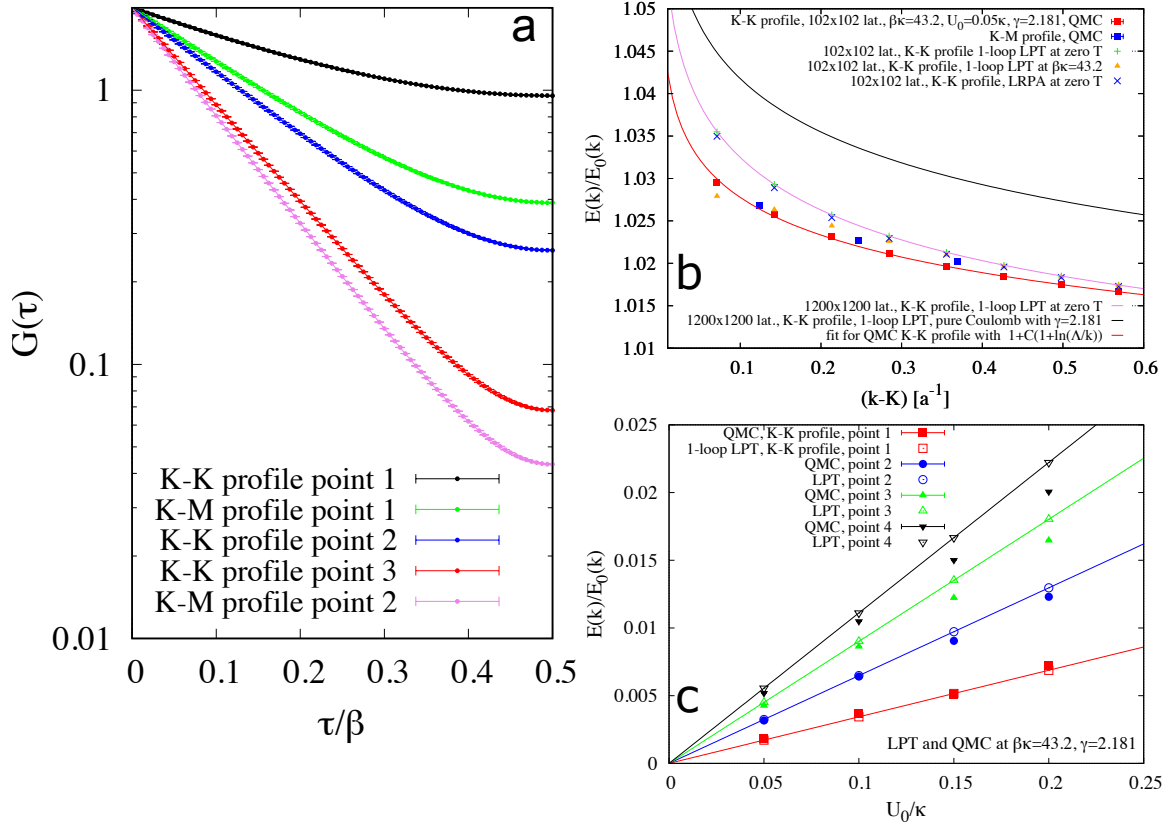


Figure S2: **(a)** QMC data for the fermion propagator in Euclidean time, $G(k, \tau)$. The computations have been performed with the interaction potential variant II, which has been rescaled in order for the on-site interaction to take the value 0.05κ (to be firmly within the weak-coupling regime). Fitting is made with the lattice ansatz (14). **(b)** Renormalized dispersion at the same coupling. In order to cross-check the QMC data, we have added the LPT results. The plot exhibits several key features. Firstly, the absence of differences between the 102×102 and 1200×1200 LPT data clearly indicates that the thermodynamic limit has been achieved. Secondly, the RPA corrections can be observed but remain quite small at this coupling. Finally, the QMC data substantially deviates from the one-loop LPT result at zero temperature. This deviation can be accounted for by finite-temperature corrections in the calculation of the one-loop electronic self-energy on the lattice. In addition to these results, we also display the LPT results at 1200×1200 for an alternate two-body potential with identical on-site interaction and γ , but all other couplings except the on-site one are defined by the Coulomb tail. This setup differs from potential variant II at intermediate distances. Nevertheless, this difference is significant enough to produce different results for the renormalized dispersion even at one-loop. This comparison serves as an additional piece of evidence that the details of the two-body interaction are important if one wishes to obtain quantitative precision. **(c)** Dependence of the renormalized dispersion on the interaction strength in the weakly-coupled regime (we rescale the potential and plot the data with respect to the rescaled on-site interaction, U_0). The QMC data clearly converge to the finite-temperature, one-loop LPT result in the limit of small interaction.

interaction takes the value $U_0 = 0.05\kappa$. We then compute the fermion propagator $G(\vec{k}, \tau)$ (6), using the QMC procedure described above. The energy renormalization is quite small in the weak-coupling regime, and thus quite high precision is needed in the measurements, typically at the level of 0.1% or more. To achieve this precision, we need to take into account corrections introduced by the Euclidean time discretization in the partition function. This discretization has consequences on the extraction of quasiparticle energies, both in terms of the reconstruction of the spectral function, as well as in terms of fitting the exponential decay of the correlators. In order to take into account the finite lattice spacing in time, we start from the following expression for the “discrete” version of the fermion propagator:

$$G_D(x, \tilde{\tau}) = \frac{\text{Tr} \{ \hat{a}_x (1 - \delta_\tau \hat{\mathcal{H}})^{\tilde{\tau}} \hat{a}_0^\dagger (1 - \delta_\tau \hat{\mathcal{H}})^{(N_\tau - \tilde{\tau})} \}}{\text{Tr} \{ (1 - \delta_\tau \hat{\mathcal{H}})^{N_\tau} \}}, \quad (10)$$

where $\tilde{\tau}$ is the integer-valued discrete Euclidean time, $\tau = \delta_\tau \tilde{\tau}$, where $\delta_\tau \equiv \beta/N_\tau$ is the step in Euclidean time. Equation (7) can then be replaced by

$$G_D(\vec{k}, \omega_n) = \int_{-\infty}^{+\infty} \frac{d\omega'}{2\pi} \frac{\rho(\vec{k}, \omega')}{1 - e^{i\omega_n \delta_\tau} (1 - \delta_\tau \omega')}, \quad (11)$$

where the fermionic Matsubara frequencies are defined as

$$\omega_n = 2\pi \frac{n+1}{N_\tau \delta_\tau}, \quad n \in \mathbb{Z}. \quad (12)$$

This leads to the replacement of the kernel in the Green-Kubo relations by the function

$$K^{(D)}(\tau, \omega) = \frac{(1 - \delta_\tau \omega)^{\tilde{\tau}}}{1 + (1 - \delta_\tau \omega)^{N_\tau}}. \quad (13)$$

The observed resonances are very narrow at small interaction strength and the QMC data quality is good enough to directly fit the correlators with the lattice versions of the exponents in the familiar Källén–Lehmann representation. Taking into account the particle-hole symmetry, and neglecting corrections of $O(\delta_\tau^2)$, equation (13) leads to the following ansatz for the fermion propagator

$$G_D(\vec{k}, \tau) = \mathcal{C} \left[(1 - \delta_\tau E)^{\tilde{\tau}} + (1 + \delta_\tau E)^{N_\tau - \tilde{\tau}} + (1 + \delta_\tau E)^{\tilde{\tau}} + (1 - \delta_\tau E)^{N_\tau - \tilde{\tau}} \right] \quad (14)$$

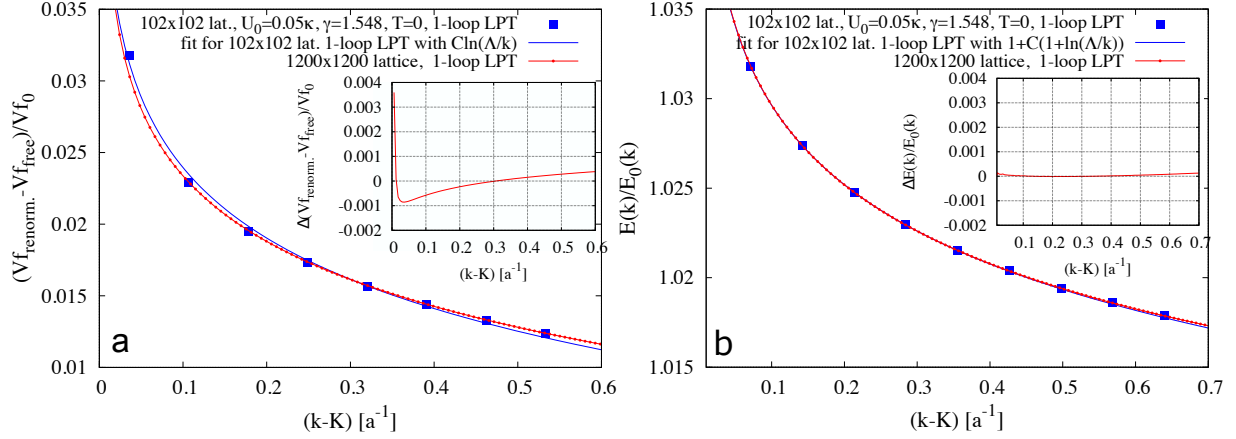


Figure S3: **(a)** Calculation of the renormalized Fermi velocity in lattice perturbation theory for small interaction: $U_0 = 0.05\kappa$ and $\gamma = 1.548$. The renormalized Fermi velocity is determined through a finite difference of neighboring points in the lattice dispersion. The difference between the logarithmic fit of the 102×102 and 1200×1200 lattice data (shown in the inset) demonstrates that there are noticeable differences arising due to the volume-limited resolution in momentum space. **(b)** The same data as in figure (a), but we now plot the dispersion relation itself. As there is no need for numerically estimating a derivative, the discrepancies between results obtained on lattices of different sizes disappear almost completely. The inset again shows the difference between the logarithmic fit of the 102×102 and 1200×1200 lattice data.

where E and C are fit parameters. Several examples of the fermion propagator at weak coupling and their fits using eq. (14) are shown in Fig. S2a. We have also checked that indeed, the lattice version of the fit performed better than its continuum counterpart. In the strong-coupling regime, the fitting form (14) becomes less reliable due to the broadening of the resonances (i.e. decrease of the particle's lifetime) and one must resort to the spectral reconstruction described in the previous section.

After fitting the correlator to (14), one obtains the values of the renormalized energies, $E(\vec{k})$. One way to obtain v_F is through numerical differentiation

$$v_F \left(\frac{k_1 + k_2}{2} \right) = \frac{E(k_1) - E(k_2)}{k_1 - k_2}, \quad (15)$$

where the momentum varies along a specific direction in the BZ. However, using this formula we introduce a systematic error of the order of $(k_1 - k_2)^2$ and also increase the statistical un-

certainties, as one is computing the difference of fluctuating quantities whose mean values only differ slightly. The analysis of the systematic errors connected with the numerical differentiation is presented in the figure [S3](#).

An alternative is to look directly at the dispersion relation $E(\vec{k})$ and modify the fitting functions. At weak coupling (and presumably at strong coupling too), the renormalization of the Fermi velocity can be decomposed as

$$v_F(\vec{k}) = v_{F,0}(\vec{k}) \left[1 + C \ln \frac{\Lambda}{|\vec{k}|} \right], \quad (16)$$

where $v_{F,0}(\vec{k})$ comes from the dispersion relation for free fermions on the hexagonal lattice. As we will work on quite large lattices, the correction to the linear dispersion will disappear once we approach the Dirac point:

$$v_{F,0}(\vec{k}) = v_{F,0}^C + \Delta_v(\vec{k}), \quad (17)$$

where $v_{F,0}^C$ is constant and $\Delta_v(\vec{k})$ is a small correction with $\lim_{|\vec{k}| \rightarrow 0} \Delta_v(\vec{k}) = 0$ (the Dirac point is placed at the origin). For most cases, we can neglect $\Delta_v(\vec{k})$ and assume $v_{F,0}(\vec{k}) = v_{F,0}^C$, but at weak coupling it is actually important to take the corrections introduced by $\Delta_v(\vec{k})$ into account due to the fact that the renormalization is quite small and is comparable with the curvature of the free band. One then integrates eq. (16) along a direction in the BZ starting from the Dirac point, taking into account that $\Delta_v(\vec{k}) = O(k)$ in its vicinity to obtain the following expression for the renormalized energy

$$\frac{E(k)}{E_0(k)} = 1 + C \left(1 + \ln \frac{\Lambda}{k} + O(k^3 \ln k) \right). \quad (18)$$

As the leading correction becomes small when approaching the Dirac point, it can be neglected and the first two terms can be used as a fitting function for the ratio of the renormalized to free dispersion. We note that if the logarithmic form (16) is violated for some reason and

we have a power law for the renormalized v_F , then the renormalized dispersion should also exhibit a power law. This would then become apparent when fitting the data. Unfortunately, we only have access to the renormalized Fermi velocity when comparing with experiment, thus we employ the procedure in eq. (15) in that case.

The results for the renormalized dispersion at small interaction are shown in Fig. S2b. As one can clearly see, perturbation theory works well in this regime as the RPA corrections to the one-loop result are quite small. The QMC data deviate substantially from the zero-temperature one-loop result, but coincide nicely with the finite-temperature one-loop lattice perturbation theory. In Fig. S2c, one can see the evolution of the renormalized dispersion with uniformly rescaled potentials. Clearly, QMC data converge to the finite-temperature one-loop approximation in the limit of small interaction.

3 Perturbation theory on the lattice

3.1 Introduction and Feynman rules

In this appendix, we discuss the details of our perturbative calculations carried out on the hexagonal lattice at finite volume, $L \equiv N_x N_y$. We start with the introduction of the lattice Hamiltonian and the Feynman rules in momentum space. We then discuss the one-loop self-energy and how we obtain the renormalized dispersion, $E_R(p)$. After this, we discuss the random phase approximation (RPA) (16), and how we have applied it to the present problem.

After performing a canonical particle-hole transformation on the fermion operators, the lattice Hamiltonian in position space can be written as

$$\hat{H} = -\kappa \sum_{\langle x,y \rangle} (\hat{a}_x^\dagger \hat{a}_y + \hat{b}_x^\dagger \hat{b}_y + \text{h.c.}) + \frac{1}{2} \sum_{x,y} V_{x,y} \hat{q}_x \hat{q}_y, \quad (19)$$

where we have introduced creation operators for electrons and holes, \hat{a}_x^\dagger and \hat{b}_x^\dagger . The charge operator appears in the interaction term and in terms of the electron and hole operators can be

written as $\hat{q}_x = \hat{a}_x^\dagger \hat{a}_x - \hat{b}_x^\dagger \hat{b}_x$. For perturbative calculations, it is convenient to go to momentum space, where (19) becomes

$$\hat{H} = \sum_{\vec{k}} \hat{\Psi}_{\vec{k}}^\dagger \hat{H}_0(\vec{k}) \hat{\Psi}_{\vec{k}} + \frac{1}{2} \sum_{\vec{k}, \mu, \nu} V_{\mu, \nu}(\vec{k}) \hat{q}_\mu(-\vec{k}) \hat{q}_\nu(\vec{k}), \quad (20)$$

with the two-body potential matrix in momentum space given by

$$V_{\mu, \nu}(\vec{k}) \equiv \sum_{\vec{r}} V_{0, \vec{r}} e^{-i\vec{k} \cdot \vec{r}}. \quad (21)$$

The sum in (21) is over the Bravais lattice vectors and the indices specify the locations of the source and sink with respect to the two sublattices. For a finite spatial volume, periodic boundary conditions in space must be imposed and this modifies the infinite-volume prescription given in (21). The charge operator in momentum space takes the form

$$\hat{q}_\mu(\vec{k}) = \sum_{\vec{q}} \left(\hat{a}_{\mu, \vec{q}-\vec{k}}^\dagger \hat{a}_{\mu, \vec{q}} - \hat{b}_{\mu, \vec{q}-\vec{k}}^\dagger \hat{b}_{\mu, \vec{q}} \right), \quad (22)$$

where we have introduced the sublattice index μ . In (20), we have written the hopping term using the following vector

$$\hat{\Psi}_{\vec{k}}^\dagger = \left(\hat{a}_{1, k}^\dagger, \hat{a}_{2, k}^\dagger, \hat{b}_{1, k}^\dagger, \hat{b}_{2, k}^\dagger \right), \quad (23)$$

with $\hat{a}_{\mu, k}^\dagger$ and $\hat{b}_{\mu, k}^\dagger$ representing particle and hole creation operators in momentum space on a given sublattice characterized by the index $\mu = 1, 2$. In this basis, the single-particle Hamiltonian takes the form

$$\hat{H}_0(\vec{k})_{a, \mu; b, \nu} = \delta_{a, b} \hat{H}_0(\vec{k})_{\mu, \nu}, \quad (24)$$

$$\hat{H}_0(\vec{k})_{1, 2} = \left(\hat{H}_0(\vec{k})_{2, 1} \right)^* = -\kappa f(\vec{k}), \quad (25)$$

where Latin indices represent the particle-hole (p-h) degree of freedom and Greek indices represent the sublattice degree of freedom. In (25), we have introduced the hexagonal lattice structure

factor

$$f(\vec{k}) \equiv \sum_{i=1,2,3} e^{i\vec{k}\cdot\vec{\delta}_i}, \quad (26)$$

where the sum runs over the three nearest-neighbor lattice vectors.

As is done on the lattice for QMC calculations, we formulate the Feynman rules using the functional integral formalism. We start with the partition function in Euclidean time after performing the Hubbard-Stratonovich transformation

$$Z = \int \mathcal{D}\phi \mathcal{D}\bar{\psi} \mathcal{D}\psi e^{-S[\bar{\psi}, \psi, \phi]}, \quad (27)$$

$$S = S_0 + S_{\text{int.}} + S_B, \quad (28)$$

$$S = \int_0^\beta d\tau \left[- \sum_{x,a} \bar{\psi}_{x,a} \partial_\tau \psi_{x,a} + \sum_{x,a;y,a} \bar{\psi}_{x,a} (H_0)_{x,a;y,b} \psi_{y,b} \right. \\ \left. + i \sum_{x,a,b} \phi_x \bar{\psi}_{x,a} \sigma_{a,b}^z \psi_{x,b} - \frac{1}{2} \sum_{x,y} \phi_x V_{x,y}^{-1} \phi_y \right], \quad (29)$$

where $\bar{\psi}$ and ψ are Grassmann fields and ϕ is a scalar field. We note that here, unlike in HMC simulations, we are working with only one, charge-coupled Hubbard field. The $U(1)$ gauge symmetry is violated by the potential matrix, $V_{x,y}$. In the limit where the $U(1)$ symmetry is restored, the Hubbard field ϕ becomes the electric field. Although we have suppressed the Euclidean time dependence of the fields in (29), the usual (anti-)periodicity applies to $(\psi)\phi$. We now write down the expressions for the propagators. The fermion propagator is defined by the expression

$$G_{x,a;y,b}(\tau) = \frac{1}{Z} \int \mathcal{D}\phi \mathcal{D}\bar{\psi} \mathcal{D}\psi \psi_{x,a}(\tau_1) \bar{\psi}_{y,b}(\tau_2) e^{-S[\bar{\psi}, \psi, \phi]}, \quad (30)$$

where $\tau \equiv \tau_1 - \tau_2$. For the free propagator, one can ignore both the interaction term and the bosonic action in (28). Going to the momentum-frequency representation, we obtain

$$G_{a,\mu;b,\nu}^{(0)}(p_0, \vec{p}) = \delta_{a,b} (\mathcal{M}^{-1}(p_0, \vec{p}))_{\mu,\nu}, \quad (31)$$

$$\begin{aligned}
& \text{(a)} \quad \text{Diagram: } \text{wavy line } q \text{ entering from left, two solid lines } p_1 \text{ and } p_2 \text{ exiting to the right, labeled } a \text{ and } b \text{ respectively.} \\
& \qquad \qquad \qquad = i\sigma_{a,b}^3 \delta^{(3)}(p_2 - p_1 - q), \quad (a) \\
& \text{(b)} \quad \text{Diagram: } \text{wavy line } q \text{ between } \mu \text{ and } \nu. \\
& \qquad \qquad \qquad = \Pi^{(0)}(\vec{q})_{\mu,\nu}, \quad (b) \\
& \text{(c)} \quad \text{Diagram: } \text{solid line } p \text{ between } \mu, a \text{ and } \nu, b. \\
& \qquad \qquad \qquad = G^{(0)}(p_0, \vec{p})_{\mu,a;\nu,b}, \quad (c)
\end{aligned}$$

Figure S4: Feynman rules in momentum-frequency representation for the action in (29). The three-component notation is used to denote the frequency and momentum dependence of each line, i.e. $p \equiv (p_0, \vec{p})$. The electron-boson vertex is shown in (a), where the Pauli matrix acts in p-h space and both momentum and frequency are conserved between the incoming and outgoing lines. The wavy line depicted in (b) corresponds to the free boson propagator and the solid line in (c) corresponds to the free fermion propagator.

where we see that the propagator is diagonal in particle/hole-space, and the matrix \mathcal{M} , which is in sublattice space, is given by

$$\mathcal{M}(p_0, \vec{p}) = \begin{pmatrix} ip_0 & -\kappa f(\vec{p}) \\ -\kappa f^*(\vec{p}) & ip_0 \end{pmatrix}. \quad (32)$$

Plugging (32) into (31) we obtain

$$G_{a,\mu;b,\nu}^{(0)}(p_0, \vec{p}) = \frac{-\delta_{a,b}}{p_0^2 + \kappa |f(\vec{p})|^2} \begin{pmatrix} ip_0 & \kappa f(\vec{p}) \\ \kappa f^*(\vec{p}) & ip_0 \end{pmatrix}_{\mu,\nu}. \quad (33)$$

The free fermion propagator will be denoted by a solid line which carries spatial momentum \vec{p} and frequency p_0 and is depicted in Fig. S4c.

The two-body interaction in our theory is mediated by the bosonic field, ϕ , which satisfies periodic boundary conditions in Euclidean time. The propagator associated with this field is defined by

$$\Pi_{x,y}(\tau) = \frac{1}{Z} \int \mathcal{D}\phi \mathcal{D}\bar{\psi} \mathcal{D}\psi \phi_x(\tau_1) \phi_y(\tau_2) e^{-S[\bar{\psi}, \psi, \phi]}, \quad (34)$$

where $\tau \equiv \tau_1 - \tau_2$. The free bosonic propagator is obtained by ignoring all terms in the action except S_B , which is Gaussian. This leads to the following expression in the momentum-frequency representation

$$\Pi_{\mu,\nu}^{(0)}(\vec{p}) = V_{\mu,\nu}(\vec{p}), \quad (35)$$

where, in the infinite-volume limit, the two-body potential in momentum space which we consider satisfies $V_{\mu,\nu}(\vec{p}) = (V_{\nu,\mu}(\vec{p}))^*$ and $V_{\mu,\nu}(\vec{p}) = (V_{\mu,\nu}(-\vec{p}))^*$. We note that (35) is independent of frequency. Here the indices refer to the sublattice degree of freedom. The free bosonic propagator will be denoted by a wavy line which carries spatial momentum \vec{p} and frequency p_0 , see Fig. S4b.

We finally come to the electron-boson interaction vertex which is determined by S_{int} . It consists of an incoming fermion line with p-h (particle-hole) index a , an outgoing fermion line with p-h index b , and a boson line. Frequency and momentum are conserved among the three lines. The vertex, depicted in Fig. S4a, is trivial in sublattice space and includes a factor of $i\sigma_{a,b}^z$ which acts in p-h space (sum over contracted p-h indices).

We comment here that so far this derivation has applied to the Euclidean version of the theory. In this case, the time variable τ , runs over a compact interval, $[0, \beta)$, and the frequencies become discrete multiples of π/β (even multiples for bosons and odd multiples for fermions). For the fermions, at $T = 0$, the only thing that would change is the replacement $p_0 \rightarrow p_0 \pm i\eta$, where $\eta = 0^+$. The infinitesimal quantity η displaces the poles from the real axis in a direction which depends on whether we are dealing with the positive or negative energy states of \hat{H}_0 , when working in the eigenbasis. In what follows, we work in the $T = 0$ but also give the results for expressions in the Matsubara formalism.



Figure S5: Diagrammatic expression of Dyson's equation for the fermion propagator. The thick line denotes the full propagator, G , the thin line denotes the free propagator, $G^{(0)}$, and the blob represents the self-energy Σ .

3.2 Renormalized dispersion at one-loop

To obtain the renormalized energy, and thus the effects of interactions on the Fermi velocity within perturbation theory, we must find the poles of the full fermion propagator in momentum-frequency representation. The full propagator is represented by all connected Feynman diagrams with one incoming and one outgoing fermion line. Typically, one considers irreducible diagrammatic quantities. For the fermion propagator, one is interested in one-particle irreducible (1PI) diagrams. These are connected diagrams with a single incoming and outgoing fermion lines which have been amputated, and which do not become disconnected after cutting a single internal fermion line. These diagrams constitute what is known as the self-energy, $\hat{\Sigma}(p_0, \vec{p})$, which is a matrix that is diagonal in p-h space and is generally not diagonal in sublattice space. Using Dyson's equation, one can express the full propagator as

$$\hat{G}^{-1}(p_0, \vec{p}) = \hat{G}_0^{-1}(p_0, \vec{p}) - \hat{\Sigma}(p_0, \vec{p}). \quad (36)$$

In terms of Feynman diagrams, (36) is depicted in Fig. S5. The poles of \hat{G} determine the quasiparticle's dispersion and this leads to the following equation

$$\begin{pmatrix} ip_0 & (\hat{G}_0^{-1} - \hat{\Sigma})_{1,2} \\ (\hat{G}_0^{-1} - \hat{\Sigma})_{2,1} & ip_0 \end{pmatrix} = 0, \quad p_0 = iE_R(\vec{p}). \quad (37)$$

Typically, this equation must be solved numerically for a fixed momentum \vec{p} in the BZ.

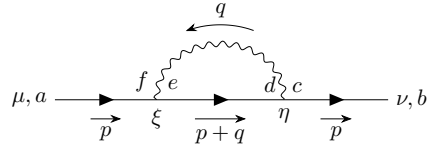


Figure S6: Diagrammatic expression for the quantity $G^{(0)}\Sigma^{(1)}G^{(0)}$, where $\Sigma^{(1)}$ is the bare first-order self-energy.

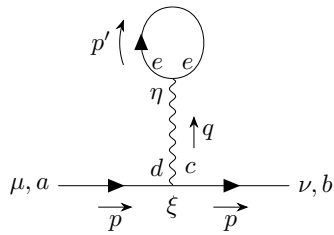


Figure S7: Diagrammatic expression for the quantity $G^{(0)}\Sigma^{(H)}G^{(0)}$, where $\Sigma^{(H)}$ is the Hartree self-energy.

The self-energy, to lowest-order, is given by the Fock diagram displayed in Fig. S6. The expression for the first-order self-energy is given by

$$\begin{aligned} \Sigma^{(1)}(p_0, \vec{p})_{f,\xi;c,\eta} = & -\frac{\delta_{c,f}}{4\pi L^2} \int dq_0 \sum_{\vec{q}} \left[\Pi_{\eta,\xi}^{(0)}(\vec{q}) G_{\xi,\eta}^{(0)}(q_0, \vec{p} + \vec{q}) \right. \\ & \left. + \Pi_{\xi,\eta}^{(0)}(\vec{q}) G_{\xi,\eta}^{(0)}(q_0, \vec{p} - \vec{q}) \right]. \end{aligned} \quad (38)$$

The sum over spatial momentum ranges over the entire Brillouin zone and the integration over all frequencies can be performed analytically. Noting that (38) does not depend on p_0 , one can easily obtain the expression for the renormalized dispersion

$$E_R(\vec{p}) = |G_{1,2}^{(0)} - \Sigma_{1,2}^{(1)}|, \quad (39)$$

$$= \left| -\kappa f(\vec{p}) + \frac{1}{4L^2} \left[\sum_{\vec{q}} \Pi_{2,1}^{(0)}(\vec{q}) e^{i\theta(\vec{k}+\vec{q})} + \sum_{\vec{q}} \Pi_{1,2}^{(0)}(\vec{q}) e^{i\theta(\vec{k}-\vec{q})} \right] \right|, \quad (40)$$

where $e^{i\theta(\vec{q})} \equiv \frac{f(\vec{q})}{|f(\vec{q})|}$. This is what we will refer to as the “bare” one-loop renormalized dispersion. The finite-temperature generalization can be obtained by inserting factors of $\tanh(|\kappa f(k \pm q)|/(2T))$ into the corresponding sums over momentum in (39). We note that the Hartree diagram (depicted in Fig. S7), which is formally the contribution of the same order as the Fock diagram, vanishes due to p-h symmetry. This symmetry would be violated with the introduction of a chemical potential or taking into account next-to-nearest neighbor hopping in the single-particle Hamiltonian, thus modifying the form of (37). The results of the first-order calculation in the weak-coupling regime are shown in Fig. S3 for various volumes. One can clearly see the logarithmic behavior of both the Fermi velocity as well as the dispersion.

3.3 Lattice RPA approximation

Although it is unreasonable to assume that one can obtain the propagator, and thus the dispersion, to all orders in perturbation theory, there are several resummations which provide good

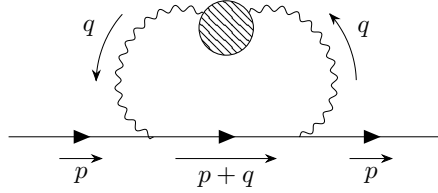


Figure S8: Diagram corresponding to the RPA self-energy. Here we have omitted the sublattice and p-h indices.

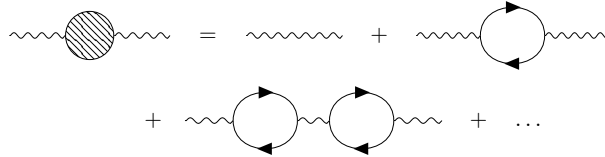


Figure S9: Diagram expression for the bosonic propagator in the RPA approximation. The polarization is calculated to first-order, which corresponds to the particle-hole bubble.

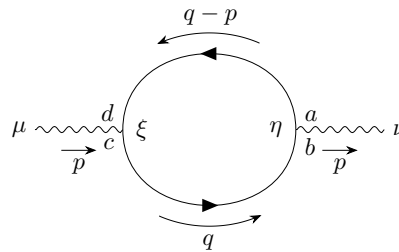


Figure S10: Diagram expression for the particle-hole bubble which is the lowest order approximation to the polarization, \hat{P} .

approximations. One such approximation is RPA, whereby one “dresses” the bare bosonic propagator and computes the diagram with the same topology as the bare self-energy (see Fig. S8). The bosonic propagator is dressed by computing the 1PI diagrams and then applying Dyson’s equation which reads

$$\hat{\Pi}(p_0, \vec{p}) = \hat{\Pi}^{(0)}(\vec{p}) \left(\mathbb{1} - \hat{P}(p_0, \vec{p}) \hat{\Pi}^{(0)}(\vec{p}) \right)^{-1}, \quad (41)$$

where the matrix-valued quantity \hat{P} is known as the polarization and contains the bosonic 1PI diagrams with two external vertices. This relation between the polarization and full bosonic propagator is depicted in Fig. S9. To lowest-order, the polarization can be represented by the particle-hole bubble depicted in Fig. S10. The expression for this quantity reads

$$P^{(1)}(p_0, \vec{p})_{\eta, \xi} = \frac{1}{2\pi L^2} \int dq_0 \sum_{\vec{q}} \left[G_{\xi, \eta}^{(0)}(q_0, \vec{q}) G_{\eta, \xi}^{(0)}(q_0 + p_0, \vec{p} + \vec{q}) + G_{\eta, \xi}^{(0)}(q_0, \vec{q}) G_{\xi, \eta}^{(0)}(q_0 - p_0, \vec{q} - \vec{p}) \right]. \quad (42)$$

The diagonal elements of $\hat{G}^{(0)}$ are identical, and thus we can write

$$P^{(1)}(p_0, \vec{p})_{1,1} = P^{(1)}(p_0, \vec{p})_{2,2} = -\frac{\kappa}{L^2} \sum_{\vec{q}}, \frac{(|f(\vec{q})| + |f(\vec{p} + \vec{q})|)}{p_0^2 + \kappa^2 (|f(\vec{q})| + |f(\vec{p} + \vec{q})|)^2}, \quad (43)$$

where the frequency integral in (42) has been performed analytically

$$\begin{aligned} I_{1,1} = I_{2,2} &\equiv \int_{-\infty}^{+\infty} dq_0 \frac{q_0(q_0 + p_0)}{(q_0^2 + \kappa^2 |f(\vec{q})|^2) ((q_0 + p_0)^2 + \kappa^2 |f(\vec{p} + \vec{q})|^2)}, \\ &= \frac{\pi \kappa (|f(\vec{q})| + |f(\vec{p} + \vec{q})|)}{p_0^2 + \kappa^2 (|f(\vec{q})| + |f(\vec{p} + \vec{q})|)^2}. \end{aligned} \quad (44)$$

The off-diagonal elements are given by

$$P^{(1)}(p_0, \vec{p})_{1,2} = \frac{\kappa}{L^2} \sum_{\vec{q}}, \frac{e^{-i\theta(q)} e^{i\theta(q+p)} (|f(\vec{q})| + |f(\vec{p} + \vec{q})|)}{p_0^2 + \kappa^2 (|f(\vec{q})| + |f(\vec{p} + \vec{q})|)^2}, \quad (45)$$

where $P_{1,2}^{(1)} = (P_{2,1}^{(1)})^*$ and the frequency integral has also been performed analytically.

$$\begin{aligned} I_{1,2} &\equiv \int_{-\infty}^{+\infty} \frac{dq_0}{(q_0^2 + \kappa^2 |f(\vec{q})|^2) ((q_0 + p_0)^2 + \kappa^2 |f(\vec{p} + \vec{q})|^2)}, \\ &= \frac{\pi (|f(\vec{q})| + |f(\vec{p} + \vec{q})|)}{\kappa |f(\vec{q})| |f(\vec{p} + \vec{q})| (p_0^2 + \kappa^2 (|f(\vec{q})| + |f(\vec{p} + \vec{q})|)^2)}. \end{aligned} \quad (46)$$

The phases $\theta(q)$ and $\theta(p+q)$ are not well-defined at the Dirac point, where the structure factor vanishes, and thus in (43) and (45), the sum over loop momenta excludes these points.

When generalizing the zero-temperature result for the polarization to $T \neq 0$, we replace the integrals over the frequency q_0 with sums over the fermionic Matsubara frequencies, $\omega_n = (2n+1)\pi/\beta$, which circulate in the particle-hole bubble. To evaluate these sums, one first expresses the sum as a contour integral in the complex plane which encloses the Matsubara frequencies on the imaginary axis. Deforming the contour in the usual such that the poles of the fermion propagators are enclosed, gives the final expression in terms of the residues at these poles. The result for the diagonal elements of the polarization tensor is given by

$$\begin{aligned}
P^{(1)}(i\Omega_n, \vec{p})_{T,\text{diag}} = & -\frac{1}{L^2} \sum_{\vec{q}}' \left[-\frac{(i\Omega_n + E_0(\vec{q})) n_F(E_0(\vec{q}))}{(i\Omega_n + E_0(\vec{q}))^2 - E_0^2(\vec{q} + \vec{p})} \right. \\
& -\frac{(i\Omega_n - E_0(\vec{q})) n_F(-E_0(\vec{q}))}{(i\Omega_n - E_0(\vec{q}))^2 - E_0^2(\vec{q} + \vec{p})} + \frac{(i\Omega_n + E_0(\vec{p} + \vec{q})) n_F(-E_0(\vec{p} + \vec{q}))}{(i\Omega_n + E_0(\vec{p} + \vec{q}))^2 - E_0^2(\vec{q})} \\
& \left. + \frac{(i\Omega_n - E_0(\vec{p} + \vec{q})) n_F(E_0(\vec{p} + \vec{q}))}{(i\Omega_n - E_0(\vec{p} + \vec{q}))^2 - E_0^2(\vec{q})} \right], \tag{47}
\end{aligned}$$

where $P_{1,1} = P_{2,2} \equiv P_{\text{diag}}$, $E_0(\vec{q}) = \kappa|f(\vec{q})|$, n_F is the Fermi function, and $\Omega_n = 2n\pi/\beta$ is a bosonic Matsubara frequency. For the off-diagonal element we obtain

$$\begin{aligned}
P^{(1)}(i\Omega_n, \vec{p})_{T,\text{off}} = & -\frac{\kappa^2}{L^2} \sum_{\vec{q}}' f(\vec{p} + \vec{q}) f^*(\vec{q}) \left[\frac{n_F(E_0(\vec{q}))}{E_0(\vec{q}) [(i\Omega_n + E_0(\vec{q}))^2 - E_0^2(\vec{q} + \vec{p})]} \right. \\
& -\frac{n_F(-E_0(\vec{q}))}{E_0(\vec{q}) [(i\Omega_n - E_0(\vec{q}))^2 - E_0^2(\vec{q} + \vec{p})]} + \frac{n_F(E_0(\vec{p} + \vec{q}))}{E_0(\vec{p} + \vec{q}) [(i\Omega_n - E_0(\vec{p} + \vec{q}))^2 - E_0^2(\vec{q})]} \\
& \left. -\frac{n_F(-E_0(\vec{p} + \vec{q}))}{E_0(\vec{p} + \vec{q}) [(i\Omega_n + E_0(\vec{p} + \vec{q}))^2 - E_0^2(\vec{q})]} \right], \tag{48}
\end{aligned}$$

where $P_{1,2} = P_{2,1}^* = P_{\text{off}}$. One can verify that these expressions reproduce (43) and (45) in the limit $T \rightarrow 0$.

Putting all of this together, we can write the fermion self-energy in the zero-temperature

RPA approximation as

$$\begin{aligned} \Sigma^{(RPA)}(p_0, \vec{p})_{f,\xi;c,\eta} = & -\frac{\delta_{f,c}}{4\pi L^2} \int dq_0 \sum_{\vec{q}} \left[\Pi(q_0, \vec{q})_{\eta,\xi} G^{(0)}(p_0 + q_0, \vec{p} + \vec{q})_{\xi,\eta} \right. \\ & \left. + \Pi(q_0, \vec{q})_{\xi,\eta} G^{(0)}(p_0 - q_0, \vec{p} - \vec{q})_{\xi,\eta} \right], \end{aligned} \quad (49)$$

where as in the bare case, the RPA self-energy is also diagonal in p-h space. From (49), one sees that the frequency integral needs to be evaluated numerically. It will be convenient to rewrite (49) in the form

$$\Sigma^{(RPA)}(p_0, \vec{p})_{f,\xi;c,\eta} = \Sigma^{(1)}(\vec{p})_{f,\xi;c,\eta} + \delta\Sigma^{(RPA)}(p_0, \vec{p})_{f,\xi;c,\eta}, \quad (50)$$

$$\begin{aligned} \delta\Sigma^{(RPA)}(p_0, \vec{p})_{f,\xi;c,\eta} \equiv & -\frac{\delta_{f,c}}{4\pi L^2} \int dq_0 \sum_{\vec{q}} \left[F(q_0, \vec{q})_{\eta,\xi} G^{(0)}(p_0 + q_0, \vec{p} + \vec{q})_{\xi,\eta} \right. \\ & \left. + F(q_0, \vec{q})_{\xi,\eta} G^{(0)}(p_0 - q_0, \vec{p} - \vec{q})_{\xi,\eta} \right], \end{aligned} \quad (51)$$

where we have introduced the matrix, $\hat{F} \equiv \hat{\Pi} - \hat{\Pi}^{(0)}$. The entire frequency dependence of $\hat{\Sigma}^{(RPA)}$ is now contained in (51). Unlike the case of the bare first-order self-energy, finding the pole of the propagator will require multiple numerical evaluations of (51) for fixed \vec{p} .

From (43) and (45), one sees that the dressed bosonic propagator depends on frequency. Before we use this in the evaluation of the RPA self-energy, we determine the frequency dependence for asymptotically large values of p_0 . We start by writing

$$\begin{aligned} \mathcal{F}(p_0, \vec{p}) & \equiv F(q_0, \vec{q})_{1,2} = \Pi(p_0, \vec{p})_{1,2} - \Pi^{(0)}(\vec{p})_{1,2}, \\ & = \frac{P_{1,2}^{(1)} \left[(\Pi_{1,1}^{(0)})^2 - (\Pi_{1,2}^{(0)})^2 \right] - \Pi_{1,2}^{(0)} (\det \hat{B} - 1)}{\det \hat{B}}, \end{aligned} \quad (52)$$

where we have defined the matrix, $\hat{B} \equiv \mathbb{1} - \hat{P}\hat{\Pi}^{(0)}$, and have used (41) in expressing the matrix elements of \hat{F} in terms of the various components of \hat{P} and $\hat{\Pi}$. Using the frequency dependence of \hat{P} , one can determine that

$$\mathcal{F}(p_0, \vec{p}) \propto \frac{1}{p_0^2 + \mathcal{C}}, \quad p_0 \rightarrow \pm\infty \quad (53)$$

where \mathcal{C} is a frequency-independent constant. Thus the frequency integral is convergent and can be evaluated numerically using standard techniques.

At nonzero- T , it turns out that performing the Matsubara sum in (51) is rather straightforward. This results from the fact that the determinant of the matrix \hat{B} , which appears in the denominator of (52), has no zeros in the complex frequency plane for any value of the momentum \vec{p} . This can be understood physically in terms of collective charge excitations in monolayer graphene (17).

As we did in the bare case, we make the replacement $p_0 = iE_R(\vec{p})$. Here we note that this is, in fact, an assumption that the pole is real and thus the lifetime of the particle is infinite. This is a feature of the RPA approximation that was seen in previous studies (18). The expression in (51), after combining the two terms, can be written as

$$\delta\Sigma_{f,1;c,2}^{(RPA)}(E_R, \vec{p}) = -\frac{\delta_{f,c}}{4\pi L^2} \int dq_0 \sum_{\vec{q}} \frac{\kappa f(\vec{p} + \vec{q}) \mathcal{F}^*(q_0, \vec{q}) (q_0^2 + \kappa^2 |f(\vec{p} + \vec{q})|^2 - E_R^2)}{(q_0^2 + \kappa^2 |f(\vec{p} + \vec{q})|^2 - E_R^2)^2 + 4q_0^2 E_R^2}, \quad (54)$$

where one can show that $\delta\Sigma_{2,1}^{(RPA)} = (\delta\Sigma_{1,2}^{(RPA)})^*$. Similarly, the expression for nonzero-temperature can be written as

$$\delta\Sigma_{f,1;c,2}^{(RPA,T)}(E_R, \vec{p}) = -\frac{\delta_{f,c}}{L^2} \sum_{\vec{q}} e^{i\theta(\vec{p}+\vec{q})} \sum_{\sigma=\pm 1, \tau=\pm 1} (-)^\sigma \mathcal{F}^*(\epsilon_{\sigma,\tau}, \vec{q}) n_F(\epsilon_{\sigma,\tau}), \quad (55)$$

$$\epsilon_{\sigma,\tau} = \epsilon_{\sigma,\tau}(\vec{q} + \vec{p}) \equiv (-)^\sigma E_R + (-)^\tau E_0(\vec{p} + \vec{q}). \quad (56)$$

Using these expressions for the zero- and nonzero-temperature self-energy, the equation which determines the pole of the fermion propagator becomes

$$E_R(\vec{p}) = |G_{1,2}^{(0)} - \Sigma_{1,2}^{(1)} - \delta\Sigma_{1,2}^{(RPA)}|, \quad (57)$$

where as is clear from (54), the RPA correction also depends on E_R . The solution to (57) can be obtained without much difficulty using fixed-point iterations for root-finding.

4 Lattice vs Continuum perturbative series

A natural question arises as to whether a comparison of our perturbative calculation in the lattice theory with the well-known results in the continuum is possible. The well-known continuum RPA results (19, 20) describe $N_f = 2$ flavors of four-component Dirac fermions in two spatial dimensions coupled to a scalar potential, A_0 , which lives in all three spatial dimensions. The action is as follows

$$S_E = - \int dt d^2x (\bar{\psi}_\alpha \gamma_0 \partial_0 \psi_\alpha + v_{0,F} \bar{\psi}_\alpha \gamma_i \partial_i \psi_\alpha + i A_0 \bar{\psi}_\alpha \gamma_0 \psi_\alpha) + \frac{1}{2e^2} \int dt d^3x (\partial_i A_0)^2, \quad (58)$$

where $v_{0,F}$ is the bare Fermi velocity and the four-dimensional gamma matrices satisfy the Clifford algebra $\{\gamma_\mu, \gamma_\nu\} = 2\delta_{\mu\nu}$. The resulting Fermi velocity renormalization in RPA approximation is also a logarithmic similar to eq. (16) with the coefficient in front of the logarithm being equal to

$$C = \frac{4}{\pi^2 N_f} (F_1(\lambda) - F_0(\lambda)), \quad (59)$$

where the rescaled coupling is $\lambda \equiv e^2 N_f / (16v_F)$ (we are using the notation of (20)) and

$$F_1(\lambda) = \begin{cases} -(\sqrt{1-\lambda^2}/\lambda) \arccos \lambda - 1 + \pi/(2\lambda) & \lambda < 1 \\ -(\sqrt{\lambda^2-1}/\lambda) \log(\lambda + \sqrt{\lambda^2-1}) - 1 + \pi/(2\lambda) & \lambda > 1 \end{cases}, \quad (60)$$

$$F_0(\lambda) = \begin{cases} -((2-\lambda^2)/(\lambda\sqrt{1-\lambda^2})) \arccos \lambda - 2 + \pi/\lambda & \lambda < 1 \\ -((\lambda^2-2)/(\lambda\sqrt{\lambda^2-1})) \log(\lambda + \sqrt{\lambda^2-1}) - 2 + \pi/\lambda & \lambda > 1 \end{cases} \quad (61)$$

We have found that the renormalized Fermi velocity obtained from (59) does not match up with that obtained from our lattice RPA calculation. In contrast, the one-loop lattice result does match the one-loop result in the continuum. This is evident in the data displayed in the main text, where a comparison is made between various perturbative results.

The deviations of continuum RPA from its LPT counterpart can be attributed to the differences between the lattice and continuum polarizations. To make this comparison, one considers

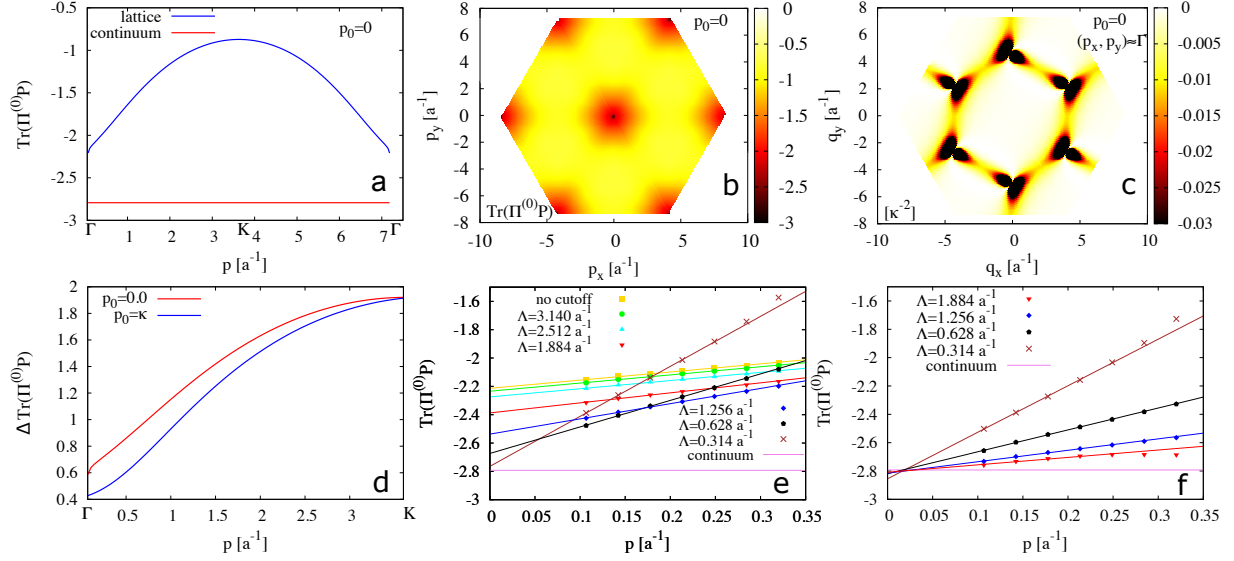


Figure S11: **(a)** Comparison of $\text{Tr}(\Pi^{(0)}P)$ computed in LPT and in the continuum. The external frequency is set to zero and the external momentum runs along the ΓK line. **(b)** Map of $\text{Tr}(\Pi^{(0)}P)$ computed in LPT within the Brillouin zone on a 102×102 lattice at zero external frequency. **(c)** Map of the summand for the lattice polarization bubble within the Brillouin zone on a 102×102 lattice. The external momenta is slightly shifted away from the Γ point and the external frequency is set to zero. The summand is concentrated around the K points, as expected. However, there is a noticeable contribution from the regions between non-equivalent, K points. **(d)** Difference between $\text{Tr}(\Pi^{(0)}P)$ computed in LPT and in the continuum theory at two values of the external frequency. **(e)** Behavior of $\text{Tr}(\Pi^{(0)}P)$ on the lattice when a cutoff in momentum around the Dirac points is introduced with the external frequency set to zero. For each line we perform a linear fit in the vicinity of zero external momentum. This shows that the continuum value of the trace, and thus the continuum dressed RPA interaction, is restored at zero momentum for a reduced cutoff. **(f)** Same as in (e) but with $\Pi^{(0)}$ computed using a linearized dispersion relation for the electrons in the polarization bubble P and using the continuum Coulomb propagator in $\Pi^{(0)}$. The continuum behavior is now restored at all momenta in the limit of large cutoff.

the dimensionless quantity $\mathcal{P} = \Pi^{(0)}P$, where P is the polarization and $\Pi^{(0)}$ is the free Coulomb propagator in the EFT. On the lattice, it corresponds to $\mathcal{P} = \text{Tr}(\Pi^{(0)}P)$, where the trace is taken over the sublattice index. This quantity, \mathcal{P} , which depends on both frequency and momentum, is examined in detail in Fig. S11. First, one notices that this quantity is simply constant in the limit of zero external frequency in the continuum theory. This is seen from the form of the

non-interacting polarization bubble in the EFT, which is given by

$$P(p_0, \vec{p}) = \frac{e^2 N_f}{8} \frac{\vec{p}^2}{\sqrt{p_0^2 + v_{F,0}^2 \vec{p}^2}}. \quad (62)$$

This constant behavior at zero frequency is not seen on the lattice, where one observes a constant shift at the Γ point with a subsequent linear dependence on external momentum (figures [S11a](#) and [b](#)). These two features are more or less independent of the external frequency, as seen in Fig. [S11d](#). To investigate this further, we plot the summand over lattice momenta for the combination of diagonal and off-diagonal elements of the lattice polarization $\Re P^{(1)}(p_0, \vec{p})_{1,2} + P^{(1)}(p_0, \vec{p})_{1,1}$ (see eq. [\(43\)](#) and [\(43\)](#)) for $p_0 = 0$ and $\vec{p} \approx 0$. This choice is determined by the fact that the numerator of the dressed bosonic propagator contains the product of the polarization and the bare Coulomb propagator [\(41\)](#), and that the diagonal and off-diagonal elements of the bare propagator are almost equal at low momenta. Thus, $\Re P^{(1)}(p_0, \vec{p})_{1,2} + P^{(1)}(p_0, \vec{p})_{1,1}$ is actually a direct analog of the continuum polarization. We see from Fig. [S11c](#) that the main contribution to the sum, which defines the lattice polarization, is still concentrated near the Dirac point, which is expected. However, there is a noticeable contribution coming from regions in between the non-equivalent Dirac points. To further investigate the origin of these differences between the continuum and the lattice polarization, one can introduce an ultraviolet cutoff in the sum over loop momentum such that only momenta within a radius Λ of the Dirac points remain. The behavior of \mathcal{P} in the vicinity of the Γ point as a function of the cutoff is shown in Fig. [S11e](#). The constant shift at the Γ point disappears in the limit of small cutoff once Λ excludes the region between the neighboring K points (see [S11c](#)). However, the linear asymptote grows with decreasing Λ . Finally, we compute P on the lattice, using the linear approximation for the dispersion relation of the electrons near the Dirac points. The resulting \mathcal{P} is shown in Fig. [S11f](#). Unlike [S11e](#), the constant shift at the Γ point does not appear at larger Λ , and the linear term also decreases with increasing cutoff, so that we finally reproduce the continuum result.

This analysis illustrates two distinct effects: first, a constant shift of \mathcal{P} at the Γ point due to inter-valley scattering, which manifests itself in the summand in the polarization loop having non-zero values in the regions between non-equivalent Dirac points; second, a cutoff effect, which results in a linear correction to \mathcal{P} around the Γ point even if the loop integrals over the two valleys are completely independent. In the next sections we discuss the possibility of including these effects into the continuum EFT.

5 Inter-valley scattering in EFT

In passing to the continuum theory, each individual fermion creation and annihilation operator in the lattice Hamiltonian can be expressed in terms of the appropriate low-energy modes. We thus introduce the following representation for the annihilation operator

$$\hat{a}_{\vec{x},\alpha,\sigma} \approx \frac{1}{L} e^{i\vec{\mathcal{K}}_1 \cdot \vec{x}} \sum_{|\vec{k}| < \Lambda} e^{i\vec{k} \cdot \vec{x}} \hat{a}_{\vec{k} + \vec{\mathcal{K}}_1, \alpha, \sigma} + \frac{1}{L} e^{i\vec{\mathcal{K}}_2 \cdot \vec{x}} \sum_{|\vec{k}| < \Lambda} e^{i\vec{k} \cdot \vec{x}} \hat{a}_{\vec{k} - \vec{\mathcal{K}}_2, \alpha, \sigma}, \quad (63)$$

where α represents the sublattice and σ represents the electron's spin. Here we have expanded the Fourier sum around the two non-equivalent Dirac points $\vec{\mathcal{K}}_1$ and $\vec{\mathcal{K}}_2$ and have cut each sum off at some large value, Λ . The expression in (63) allows us to introduce new operators which vary slowly over the unit cell

$$\hat{a}_{\sigma, \vec{r}, \nu} = e^{i\vec{\mathcal{K}}_1 \cdot \vec{r}} \hat{\psi}_{\sigma, \vec{r}, \nu}^1 + e^{i\vec{\mathcal{K}}_2 \cdot \vec{r}} \hat{\psi}_{\sigma, \vec{r}, \nu}^2, \quad (64)$$

where $\hat{\psi}_{\sigma, \vec{r}, \nu}^\mu$ is a component the four-component Dirac spinor

$$\hat{\psi}_{\sigma, \vec{r}} = (\hat{\psi}_{\sigma, \vec{r}, 1}^1, \hat{\psi}_{\sigma, \vec{r}, 2}^1, \hat{\psi}_{\sigma, \vec{r}, 1}^2, \hat{\psi}_{\sigma, \vec{r}, 2}^2), \quad (65)$$

with ν representing the sublattice and the superscript denoting the valley. In order to describe the ‘‘tunneling’’ between a given Dirac point and all three of its neighbouring, non-equivalent Dirac points (see Fig. S11c), we rewrite (65) in the form

$$\hat{a}_{\sigma, \vec{r}, \nu} = \frac{1}{3} (e^{i\vec{\mathcal{K}}_1 \cdot \vec{r}} + e^{i\vec{\mathcal{K}}_1' \cdot \vec{r}} + e^{i\vec{\mathcal{K}}_1'' \cdot \vec{r}}) \hat{\psi}_{\sigma, \vec{r}, \nu}^1 + \frac{1}{3} (e^{i\vec{\mathcal{K}}_2 \cdot \vec{r}} + e^{i\vec{\mathcal{K}}_2' \cdot \vec{r}} + e^{i\vec{\mathcal{K}}_2'' \cdot \vec{r}}) \hat{\psi}_{\sigma, \vec{r}, \nu}^2, \quad (66)$$

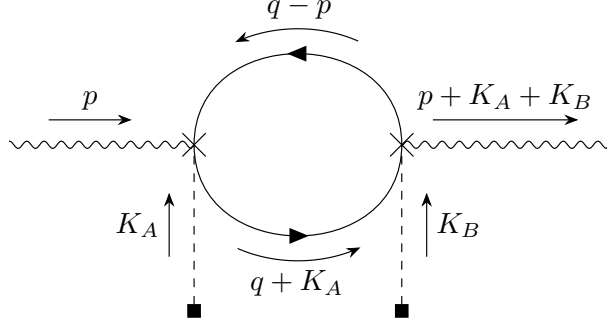


Figure S12: Correction to the polarization P , arising from inter-valley scattering.

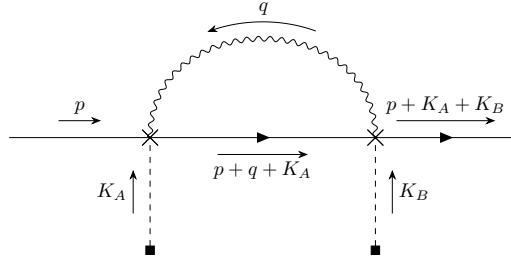


Figure S13: Correction to the self energy, arising from inter-valley scattering.

where $\vec{\mathcal{K}}'_i = \vec{\mathcal{K}}_i + \vec{b}_1$ and $\vec{\mathcal{K}}''_i = \vec{\mathcal{K}}_i - \vec{b}_2$ are equivalent Dirac points.

We apply this transformation to the electron-electron interaction between unit cells separated by a distance $\vec{\Delta}$

$$\sum_{\nu, \nu'} V_{\vec{x}, \vec{x} + \vec{\Delta}} q_{\vec{x}, \nu} q_{\vec{x} + \vec{\Delta}, \nu'}, \quad (67)$$

where we assume that $|\vec{\Delta}|$ is large compared with the lattice spacing. In this case, the diagonal and off-diagonal elements of the interaction in sublattice space are nearly identical and thus we can sum over the sublattice indices, ν and ν' . This procedure leads to the modification of the

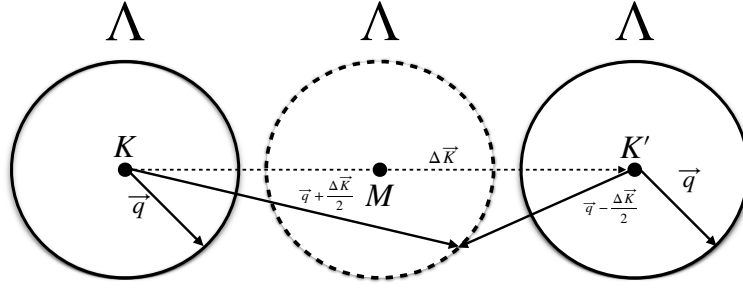


Figure S14: Integration region for the contribution to the polarization stemming from the modified continuum charged current. Each circle represents a region in momentum space of radius Λ , centered around the two Dirac points and the M point, respectively.

expression for the charged current in the EFT

$$\tilde{j}_0 = \bar{\psi}_a \gamma_0 (I + \sum_j e^{(-i\vec{x} \cdot \Delta \vec{\mathcal{K}}_j \tau_3 / 2)} \tau_1 e^{(i\vec{x} \cdot \Delta \vec{\mathcal{K}}_j \tau_3 / 2)}) \psi_a, \quad (68)$$

where τ_j are Pauli matrices in valley space and $\Delta \vec{\mathcal{K}}_j$, $j = 1, 2, 3$ are the lattice vectors which connect a single Dirac point with its three neighbouring, non-equivalent Dirac points.

We finally insert this expression into the polarization in order to see how the continuum expression is modified. We note that the additional term in the current can be written in a more compact way

$$e^{(-i\vec{x} \cdot \Delta \vec{\mathcal{K}}_j \tau_3 / 2)} \tau_1 e^{(i\vec{x} \cdot \Delta \vec{\mathcal{K}}_j \tau_3 / 2)} = \tau_+ e^{i\vec{x} \cdot \Delta \vec{\mathcal{K}}_j} + \tau_- e^{-i\vec{x} \cdot \Delta \vec{\mathcal{K}}_j}, \quad (69)$$

where $\tau_+ = \frac{1}{2}(\tau_1 + \tau_2)$ and $\tau_- = \frac{1}{2}(\tau_1 - \tau_2)$ are matrices acting in valley space. The additional term generates a shift of the momentum at the vertex due to the oscillating exponents, which is accompanied by a jump between the valleys. The corresponding diagram is depicted in Fig. S12 with $\vec{K}_A, \vec{K}_B = \pm \Delta \vec{\mathcal{K}}_j$. We are, however, only interested in the diagram where the total momentum is conserved, and thus $\vec{K}_A = -\vec{K}_B$. The additional terms in the polarization which are generated by the modified vertex are given by

$$\delta P_j^{(I)}(p_0, \vec{p}) = \int \frac{dq_0 d\vec{q}}{(2\pi)^3} \text{Tr} \left[\gamma_0 \tau_- G(p_0 + q_0, \vec{p} + \vec{q} + \Delta \vec{\mathcal{K}}_j / 2) \gamma_0 \tau_+ G(q_0, \vec{q} - \Delta \vec{\mathcal{K}}_j / 2) \right], \quad (70)$$

where

$$G(p_0, \vec{p}) = \frac{p_0 \gamma_0 + \vec{p} \cdot \vec{\gamma} v_{F,0}}{p_0^2 + \vec{p}^2 v_{F,0}^2} \quad (71)$$

is the continuum Euclidean fermion propagator. We choose the following basis for the γ matrices

$$\gamma_0 = \begin{pmatrix} \sigma_3 & 0 \\ 0 & \sigma_3 \end{pmatrix}, \quad \gamma_1 = \begin{pmatrix} \sigma_2 & 0 \\ 0 & -\sigma_2 \end{pmatrix}, \quad \gamma_2 = \begin{pmatrix} \sigma_1 & 0 \\ 0 & \sigma_1 \end{pmatrix}, \quad \gamma_3 = \begin{pmatrix} 0 & \sigma_2 \\ \sigma_2 & 0 \end{pmatrix}, \quad (72)$$

where the Pauli matrices σ_i act in sublattice space. The presence of the τ_{\pm} matrices implies that only inter-valley terms contribute when performing the trace. If take the origin of the momenta in the fermion propagators to reside at the neighbouring non-equivalent Dirac points (different valleys), the resulting integral will be centered exactly around the M point, as shown in figure [S14](#). Evaluating (70) gives the expression

$$\delta P_j^{(I)}(p_0, \vec{p}) \sim \frac{p_0^2 + (p_1 + (\Delta \mathcal{K}_j)_1)^2}{\sqrt{p_0^2 + v_{F,0}^2 (\vec{p} + \Delta \vec{\mathcal{K}}_j)^2}} + \frac{p_0^2 + (p_1 - (\Delta \mathcal{K}_j)_1)^2}{\sqrt{p_0^2 + v_{F,0}^2 (\vec{p} - \Delta \vec{\mathcal{K}}_j)^2}} \quad (73)$$

which clearly violates the rotational symmetry of the EFT. The problem arises due to the fact that the linear, low-energy approximation to the lattice propagator $G(p_0, \vec{p})$ (71) is not appropriate for (70), since shifts in momentum space $\Delta \vec{\mathcal{K}}_j$ are quite large and on the order of the cutoff. This means that we need to add higher-dimensional kinetic terms to the QED Lagrangian in order to reproduce the dispersion relation around the M point and thus obtain a better description for inter-valley scattering.

As, with the polarization, the modified current also gives a contribution to the one-loop self energy (Fig. [S13](#))

$$\delta \Sigma_j^{(I)}(p_0, \vec{p}) = \int \frac{dq_0 d\vec{q}}{(2\pi)^3} \gamma_0 \tau_- G(q_0, \vec{q}) \gamma_0 \tau_+ \frac{1}{\vec{p} - \vec{q} - \Delta \vec{\mathcal{K}}_j} \sim p \ln \frac{\Lambda}{|\vec{p} - \Delta \vec{\mathcal{K}}_j|}. \quad (74)$$

Again, we only consider diagrams where the total momentum is conserved, $\vec{K}_A = -\vec{K}_B$. Due to the momentum shift, the correction to v_F is proportional to $\ln \frac{\Lambda}{|\vec{p} - \Delta \vec{\mathcal{K}}_j|}$, which goes like $\ln \frac{\Lambda}{\Delta \mathcal{K}_j} +$

$O(|\vec{p}|/\Delta\mathcal{K}_j)$ in the limit $|\vec{p}| \rightarrow 0$. The constant can be absorbed into the cutoff, and the resulting corrections to the Fermi velocity are suppressed, as they are $O(|\vec{p}|/\ln|\vec{p}|)$ with respect to the leading logarithmic divergence of v_F . One can thus conclude that these corrections from the modified current are considerably smaller for the one-loop self-energy than for the polarization (73).

6 Comment on regularization of UV divergences

We comment here on the effects due to the finite cutoff and on the choice of regularization scheme used in continuum perturbative calculations. We also discuss the implications for lattice perturbation theory as well as QMC.

Previous studies in the continuum have typically relied on dimensional regularization for the calculation of divergent integrals. The most notable example is the polarization bubble, which is naively linearly divergent. On the lattice, however, one introduces an intrinsic ultraviolet cutoff of the order of the inverse lattice spacing, $\Lambda \sim a^{-1}$. It is well-known that in QED, such a hard cutoff introduces inconsistencies. This is due to the violation of the Ward identity which results from the photon receiving a mass proportional to the cutoff, $m_\gamma \propto e\Lambda$ in $(3+1)$ dimensions (21). As a result, dimensional regularization, or even Pauli-Villars, are preferable regularization schemes in this case. These same issues were debated previously in many-body perturbative calculations where the linear approximation to the dispersion around the Dirac points has been used (22, 23), especially in the calculation of the conductivity of graphene.

Here, motivated by the comparison with LPT and QMC data, we still argue that a hard cutoff scheme should be used. The violation of the Ward identities is not really a problem if we are interested in reproducing LPT results. In fact, the lattice polarization does not have the general form $P \sim \vec{k}^2 F(k)$, as it contains inter-valley scattering and finite-cutoff effects. To keep the theory self-consistent, we should modify the current according to (68). It is thus natural to

ignore the violation of the naive Ward identities as they hold in QED due to the fact that the relation $\partial_\mu j^\mu = 0$ no longer holds.

Below, we show that the introduction of a finite cutoff leads to exactly the same effects in the polarization which we observed during the comparison of the continuum and LPT results. We start from the ordinary polarization bubble (Fig. [S10](#)) in the EFT and first perform the integration over the loop frequency q_0 to get

$$P^{(\Lambda)}(p_0, \vec{p}) = 2N_f v_{F,0} \int_0^\Lambda \frac{d\vec{q}}{(2\pi)^2} \left(\frac{|\vec{q}| + v_{F,0} |\vec{q} + \vec{p}|}{p_0^2 + v_{F,0}^2 (|\vec{q}| + |\vec{q} + \vec{p}|)^2} \right) \left(1 - \frac{\vec{q}(\vec{p} + \vec{q})}{|\vec{q}| |\vec{q} + \vec{p}|} \right). \quad (75)$$

Note that the cutoff is imposed only on the spatial components of the loop momenta and the integral over frequencies is taken over the entire real axis. Instead of exactly computing the integral in [\(75\)](#), we use the fact that it is convergent in the limit $\Lambda \rightarrow \infty$ which is evident from the continuum expression in [\(62\)](#). Thus, we can write

$$P^{(\Lambda)}(p_0, \vec{p}) = P(p_0, \vec{p}) + \delta P^{(\Lambda)}(p_0, \vec{p}), \quad (76)$$

where the first term on the right-hand side of [\(76\)](#) is identical to [\(62\)](#), which was computed in dimensional regularization. The correction $\delta P^{(\Lambda)}(p_0, \vec{p})$ can be expanded in powers of Λ^{-1} :

$$\delta P^{(\Lambda)}(p_0, \vec{p}) = -\frac{N_f}{v_{F,0}} \frac{7}{16\pi} \frac{\vec{p}^2}{\Lambda} + O(\Lambda^{-2}), \quad (77)$$

where the first correction due to the hard cutoff is frequency independent, while the higher-order terms will, in general, depend on frequency. This correction multiplied by the bare Coulomb propagator, which is proportional to $\sim 1/|\vec{p}|$ gives the term proportional to $\sim |\vec{p}|$ near the Γ point, exactly as we saw in the figures [S11a](#) and [S11d-f](#). The coefficient in front of this term disappears in the limit $\Lambda \rightarrow 0$ exactly as predicted in [S11f](#).

The same technique can be also applied to the bare first-order fermion self-energy. Note that we can not shift the loop momentum after the introduction of the Feynman parameters as

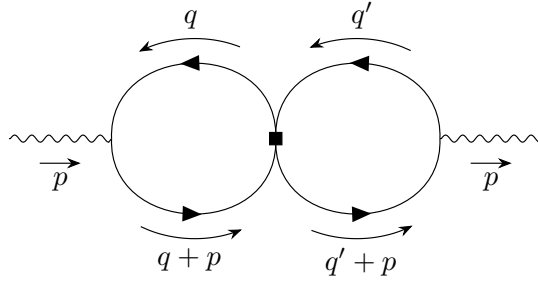


Figure S15: Lowest-order correction to the polarization P , arising due to the addition of four-Fermi terms in the low-energy continuum action.

is usually done. Performing this calculation we obtain the usual one-loop leading term

$$\Sigma(p_0, \vec{p}) = v_{F,0} \gamma_i p_i \frac{\alpha}{4} \log \left(\frac{\Lambda}{|\vec{p}|} \right), \quad (78)$$

and corrections

$$\delta \Sigma^{(\Lambda)}(p_0, \vec{p}) = v_{F,0} \gamma_i p_i \left(C_0 + C_1 \frac{|\vec{p}|^2}{\Lambda^2} + O \left(\frac{|\vec{p}|^4}{\Lambda^4} \right) \right). \quad (79)$$

We note that the hard cutoff does not generate a term in the self-energy proportional to $k_0 \gamma_0$ at this order. The constant C_0 can be absorbed in the cutoff and thus the leading correction is $O(|\vec{p}|^2/\Lambda^2)$. It is again smaller than the correction to the polarization, which is consistent with the appearance of the lattice corrections starting at the RPA level when comparing the continuum calculations to LPT and QMC data.

7 Four-Fermi terms in the continuum EFT

Another way to modify the EFT is to add higher-dimensional operators (24). One can write down twelve four-Fermi operators, each having a mass-dimension of four and are thus “irrelevant” in the RG sense. For completeness, we write down the general form of these terms in the

Euclidean action

$$S_{\text{E,int}} = \frac{u_i}{2N_f} \int dt d^2x (\bar{\psi}_\alpha \Gamma_i \psi_\alpha)^2, \quad (80)$$

where the coupling u_i is proportional to the inverse UV cutoff, α is a flavor index, and Γ_i determines the vertex structure in spinor space. Taking into account the structure of the four-component Dirac spinor (64) and the fact that only the γ_3 matrix is non-diagonal in valley space (72), the obvious candidates for the the description of inter-valley scattering are the terms of the form $\Gamma_i = \gamma_3 \tilde{\Gamma}_i$, where $\tilde{\Gamma}_i \in \{1, \gamma_0, \gamma_i, \gamma_5, \gamma_0 \gamma_i, \gamma_0 \gamma_5\}$ and $\gamma_5 \equiv \gamma_0 \gamma_1 \gamma_2$.

The polarization in the continuum Dirac field theory receives a contribution at linear order in each u_i , which is depicted in Fig. S15. These diagrams represent two terms, a single-trace term and a double-trace term

$$P^{(u)}(p_0, \vec{p}) = P_a^{(u)}(p_0, \vec{p}) + P_b^{(u)}(p_0, \vec{p}), \quad (81)$$

where

$$P_a^{(u)}(p) = u_i \frac{e^2}{v_F^2} N_f \int \frac{d^3q}{(2\pi)^3} \text{Tr} (G(q+p) \gamma_0 G(q) \Gamma_i) \int \frac{d^3q'}{(2\pi)^3} \text{Tr} (G(q'+p) \Gamma_i G(q') \gamma_0), \quad (82)$$

$$P_b^{(u)}(p) = -u_i \frac{e^2}{v_F^2} \int \int \frac{d^3q}{(2\pi)^3} \frac{d^3q'}{(2\pi)^3} \text{Tr} (G(q) \Gamma_i G(q') \gamma_0 G(q'+p) \Gamma_i G(q+p) \gamma_0). \quad (83)$$

Here we use the ‘‘relativistic’’, four-vector notation $q = (q_0, v_F \vec{q})$ for all momenta, while the trace is performed over spinor indices with the appropriate powers of N_f resulting from tracing over flavor indices. We show in detail how the integrals are computed for the four-Fermi term associated with $\Gamma_i = \gamma_3$ and simply state the final results for the other terms.

One can easily show that (82) vanishes due to the fact that γ_3 is block off-diagonal while the remaining gamma matrices are all block-diagonal. This also holds true for all other couplings involving γ_3 . To evaluate (83), we note that the two loop integrals factor and thus the term takes the form

$$P_b^{(u)}(p) = -u_i \frac{e^2}{v_F^2} \tilde{\epsilon}_{\mu\nu\kappa\lambda} I(p)_{\mu\nu} I(p)_{\kappa\lambda}, \quad (84)$$

where we have introduced

$$\tilde{\epsilon}_{\mu\nu\kappa\lambda} \equiv \text{Tr} (\gamma_\mu \gamma_0 \gamma_\nu \gamma_3 \gamma_\lambda \gamma_0 \gamma_\kappa \gamma_3), \quad (85)$$

and

$$I(p)_{\mu\nu} \equiv \int \frac{d^3q}{(2\pi)^3} \frac{(q+p)_\mu q_\nu}{(q+p)^2 q^2}. \quad (86)$$

Using the fact that the matrix γ_3 anticommutes with all other gamma matrices together with the identity $\text{Tr} (\gamma_\mu \gamma_\nu \gamma_\kappa \gamma_\lambda) = 4(\delta_{\mu\nu} \delta_{\kappa\lambda} - \delta_{\mu\kappa} \delta_{\nu\lambda} + \delta_{\mu\lambda} \delta_{\nu\kappa})$, one can evaluate (85). The result is given by

$$\begin{aligned} \tilde{\epsilon}_{\mu\nu\kappa\lambda} = & -4(\delta_{\mu\nu} \delta_{\lambda\kappa} - \delta_{\mu\lambda} \delta_{\nu\kappa} + \delta_{\mu\kappa} \delta_{\nu\lambda}) + 8\delta_{0\lambda} (\delta_{\mu\nu} \delta_{0\kappa} - \delta_{\mu 0} \delta_{\nu\kappa} + \delta_{\mu\kappa} \delta_{\nu 0}) \\ & - 8\delta_{0\nu} (\delta_{\mu\lambda} \delta_{0\kappa} - \delta_{\mu 0} \delta_{\lambda\kappa} + \delta_{\mu\kappa} \delta_{\lambda 0}), \end{aligned} \quad (87)$$

To compute the integral over the loop momentum in (86) using dimensional regularization, one uses the standard procedure of combining the factors in the denominator using Feynman parameters, shifting the loop momentum to make the denominator an even function of q , and then dropping terms in the numerator which are linear in q . The result of this procedure can be written as

$$I(p)_{\mu\nu} = -\frac{\sqrt{p^2}}{64} \left(\delta_{\mu\nu} + \frac{p_\mu p_\nu}{p^2} \right). \quad (88)$$

Now, contracting this expression with the tensor (87) we obtain the result

$$P_{(\gamma_3)}^{(u)}(p_0, \vec{p}) = \frac{u_1 e^2}{256 v_F^2} \vec{p}^2. \quad (89)$$

The correction in (89) is quadratic in spatial momentum, thus it contributes to the linear term in \mathcal{P} , but does not affect the constant shift near the Γ point (see Fig. S11a). As we discussed previously, the linear term in the lattice polarization is a lattice cutoff effect, while inter-valley

scattering is responsible for the constant shift at the Γ point. All of this implies that the $\Gamma_i = \gamma_3$ four-Fermi term cannot describe the inter-valley scattering which we see in the lattice polarization.

We proceed with the contributions from the remaining five terms which couple the two Dirac points. The calculations are similar to those performed above and the results are

$$P_{(\gamma_0\gamma_3)}^{(u)}(p_0, \vec{p}) = -\frac{u_2 e^2}{256 v_F^2} (\vec{p}^2 - p_0^2) \left(1 - \frac{p_0^2}{p^2}\right), \quad (90)$$

$$P_{(i\gamma_3\gamma_5)}^{(u)}(p_0, \vec{p}) = \frac{u_3 e^2}{256 v_F^2} \vec{p}^2, \quad (91)$$

$$P_{(i\gamma_3\gamma_i)}^{(u)}(p_0, \vec{p}) = -\frac{2u_4 e^2}{256 v_F^2} \vec{p}^2 \left(1 - \frac{p_0^2}{p^2}\right), \quad (92)$$

$$P_{(i\gamma_3\gamma_0\gamma_5)}^{(u)}(p_0, \vec{p}) = \frac{u_5 e^2}{256 v_F^2} (\vec{p}^2 - p_0^2) \left(1 - \frac{p_0^2}{p^2}\right), \quad (93)$$

$$P_{(i\gamma_3\gamma_0\gamma_i)}^{(u)}(p_0, \vec{p}) = \frac{2u_6 e^2}{256 v_F^2} \vec{p}^2 \left(1 - \frac{p_0^2}{p^2}\right). \quad (94)$$

Thus, one can see that these four-Fermi operators also contribute to the linear term in \mathcal{P} , but do not affect the constant shift at the Γ point.

An additional problem is that the other six four-Fermi terms which do not involve γ_3 also contribute to the polarization at this order. For the operators corresponding to γ_0 and γ_i , both the single-trace term and double-trace term are nonzero. The final contributions to the polarization

are as follows

$$P_{(\mathbb{1})}^{(u)}(p_0, \vec{p}) = -\frac{u_7 e^2}{256 v_F^2} \vec{p}^2, \quad (95)$$

$$P_{(\gamma_0)}^{(u)}(p_0, \vec{p}) = \frac{u_8 e^2}{256 v_F^2} \left\{ -(\vec{p}^2 - p_0^2) \left(1 - \frac{p_0^2}{p^2} \right) + 4N_f \vec{p}^2 \right\}, \quad (96)$$

$$P_{(i\gamma_5)}^{(u)}(p_0, \vec{p}) = \frac{u_9 e^2}{256 v_F^2} \vec{p}^2, \quad (97)$$

$$P_{(i\gamma_0\gamma_5)}^{(u)}(p_0, \vec{p}) = -\frac{u_{10} e^2}{256 v_F^2} (\vec{p}^2 - p_0^2) \left(1 - \frac{p_0^2}{p^2} \right), \quad (98)$$

$$P_{(\gamma_i)}^{(u)}(p_0, \vec{p}) = \frac{u_{11} e^2}{256 v_F^2} \left(2\frac{\vec{p}^4}{p^2} + 4N_f \frac{p_0^2 \vec{p}^2}{p^2} \right), \quad (99)$$

$$P_{(\gamma_0\gamma_i)}^{(u)}(p_0, \vec{p}) = \frac{2u_{12} e^2}{256 v_F^2} p^2 \left(3 + \frac{p_0^4}{p^4} \right). \quad (100)$$

Disentangling each of these contributions and their relation to the lattice polarization is a difficult task. For instance, it is not possible to distinguish the contributions $P_{(\mathbb{1})}^{(u)}$ and $P_{(\gamma_3)}^{(u)}$. One thus requires additional information in order to fix the inclusion of the four-Fermi terms in the continuum EFT.

It is known, however, that four-Fermi terms can actually play a different role in the EFT. Previous studies have shown that short-range interactions on the hexagonal lattice can generate some of the four-Fermi terms enumerated above once one passes to the low-energy continuum EFT (25). We now list the terms generated by the on-site Hubbard interaction as well as the nearest-neighbor interaction.

The Hubbard interaction on the hexagonal lattice can be written as

$$\hat{H}_U = \frac{U}{4} \sum_x \left\{ (\hat{n}_{x,A} + \hat{n}_{x,B})^2 + (\hat{n}_{x,A} - \hat{n}_{x,B})^2 \right\}, \quad (101)$$

where the sum runs over the unit cells of the lattice and we have introduced the number operator, $\hat{n}_{x,A} \equiv \hat{a}_{x,A,\uparrow}^\dagger \hat{a}_{x,A,\uparrow} + \hat{a}_{x,A,\downarrow}^\dagger \hat{a}_{x,A,\downarrow}$, restricted to sublattice A with the same operator $\hat{n}_{x,B}$ on sublattice B . As shown previously, the fermion operators can be expressed in terms of the degrees of freedom of the low-energy EFT (64). We apply this transformation to (101), and

drop oscillating terms which contain $\cos(\Delta\vec{\mathcal{K}}_j\vec{x})$ or $\sin(\Delta\vec{\mathcal{K}}_j\vec{x})$, as they are sub-leading at low energies. The first term in (101), can be expressed as

$$\sum_{\alpha} \int d^2x \left\{ (\bar{\psi}_{\alpha}\gamma_0\psi_{\alpha})^2 - \frac{1}{2}(\bar{\psi}_{\alpha}\gamma_2\gamma_3\psi_{\alpha})^2 - \frac{1}{2}(\bar{\psi}_{\alpha}\gamma_0\gamma_1\gamma_3\psi_{\alpha})^2 \right\}, \quad (102)$$

where the sum runs over spin and we have passed to the continuum limit by replacing the sum with an integral, $a^2 \sum_x \sim \int d^2x$, where a is the lattice spacing of the hexagonal lattice. In a similar way, the second term in (101) can be written as

$$\sum_{\alpha} \int d^2x \left\{ (\bar{\psi}_{\alpha}\psi_{\alpha})^2 - \frac{1}{2}(\bar{\psi}_{\alpha}\gamma_0\gamma_2\gamma_3\psi_{\alpha})^2 - \frac{1}{2}(\bar{\psi}_{\alpha}\gamma_1\gamma_3\psi_{\alpha})^2 \right\}. \quad (103)$$

Putting together (102) and (103), one can see that the following four-Fermi terms are added to the low-energy action by the Hubbard interaction

$$S_U = G_U \sum_{\alpha} \int d^2x \left\{ (\bar{\psi}_{\alpha}\psi_{\alpha})^2 + (\bar{\psi}_{\alpha}\gamma_0\psi_{\alpha})^2 - \frac{1}{2}(\bar{\psi}_{\alpha}\gamma_i\gamma_3\psi_{\alpha})^2 - \frac{1}{2}(\bar{\psi}_{\alpha}\gamma_0\gamma_i\gamma_3\psi_{\alpha})^2 \right\}, \quad (104)$$

where we have introduced the effective coupling G_U , which has a negative mass dimension and is proportional to the Hubbard interaction U in (101).

The nearest-neighbor density-density interaction also plays a role in the low-energy continuum action. The lattice interaction Hamiltonian can be written as follows

$$\hat{H}_V = \frac{V}{4} \sum_{\vec{\delta}_i} \sum_x \left\{ (\hat{n}_{x,A} + \hat{n}_{x+\vec{\delta}_i,B})^2 - (\hat{n}_{x,A} - \hat{n}_{x+\vec{\delta}_i,B})^2 \right\}, \quad (105)$$

where the first sum runs over the three nearest-neighbor vectors $\vec{\delta}_i$. Repeating the same steps as for the on-site interaction and then summing over the nearest-neighbor vectors, one obtains

$$S_V = G_V \sum_{\alpha} \int d^2x \left\{ (\bar{\psi}_{\alpha}\gamma_0\psi_{\alpha})^2 - (\bar{\psi}_{\alpha}\psi_{\alpha})^2 \right\}, \quad (106)$$

where we have introduced the effective coupling G_V arising from the nearest-neighbor interaction.

We have thus seen how a subset of the allowed four-Fermi operators in the continuum effective field theory naturally arise from the short-range interactions inherent in our many-body Hamiltonian. However, it has been previously shown that the fermion self-energy receives only small corrections due to local interactions and the higher-dimensional operators that they generate in the continuum (26). This is confirmed by QMC and higher-order LPT data, where we have found that these couplings modify the fitted value of the cutoff and do not affect the coefficient in front of the logarithm in the expression for the renormalized Fermi velocity.

Another, simpler approach that modifies the EFT is to simply absorb lattice-scale physics as well as possible higher-order perturbative corrections into a “renormalized” coupling constant. This procedure excludes a mapping of the microscopic details of the lattice theory to the continuum theory. In general, with the modification of a single constant α , one can not fully absorb all corrections coming from lattice-scale physics. However, in the particular case of the renormalization of v_F , which boils down to a single coefficient in front of the logarithm, this procedure seems reasonable. If we use the one-loop expression for v_F in the EFT 78 and match it to lattice RPA (potential variant II), we get $\alpha_{renorm.}^{(1)} = 1.372$. Doing the same with QMC yields $\alpha_{renorm.}^{(2)} = 0.626$, and thus we see a substantial reduction in the “renormalized” coupling in comparison with its bare value $\alpha = 2.504$ in suspended graphene. We can in principle perform this matching also at the level of the continuum RPA, providing that the QMC coefficient C does not exceed $2/\pi^2$, which is the saturation value of the expression 59 for continuum RPA. This is true for at least low-temperature data, though the high-temperature data falls outside of this limit (as seen in Fig. 2 of the main text). Thus it is unlikely that one can obtain a satisfactory fit of finite-temperature effects with this approach while also signaling that the continuum theory is not useful beyond the one-loop level.

References

1. M. V. Ulybyshev, P. V. Buividovich, M. I. Katsnelson, M. I. Polikarpov, *Phys. Rev. Lett.* **111**, 056801 (2013).
2. D. Smith, L. von Smekal, *Phys. Rev. B* **89**, 195429 (2014).
3. M. Ulybyshev, C. Winterowd, S. Zafeiropoulos, *Phys. Rev. B* **96**, 205115 (2017).
4. P. Buividovich, D. Smith, M. Ulybyshev, L. von Smekal, *Phys. Rev. B* **99**, 205434 (2019).
5. M. Ulybyshev, C. Winterowd, S. Zafeiropoulos, *Phys. Rev. D* **101**, 014508 (2020).
6. C. Wu, S.-C. Zhang, *Phys. Rev. B* **71**, 155115 (2005).
7. R. Blankenbecler, D. J. Scalapino, R. L. Sugar, *Phys. Rev. D* **24**, 2278 (1981).
8. M. Hohenadler, F. Parisen Toldin, I. F. Herbut, F. F. Assaad, *Phys. Rev. B* **90**, 085146 (2014).
9. H.-K. Tang, *et al.*, *Science* **361**, 570 (2018).
10. T. DeGrand, C. DeTar, *Lattice Methods for Quantum Chromodynamics* (World Scientific, 2006).
11. T. Stauber, *et al.*, *Phys. Rev. Lett.* **118**, 266801 (2017).
12. J.-L. Wynn, E. Berkowitz, C. Körber, T. A. Lähde, T. Luu, *Phys. Rev. B* **100**, 075141 (2019).
13. K. S. D. Beach, *arXiv e-prints* pp. cond-mat/0403055 (2004).
14. M. Bercx, F. Goth, J. S. Hofmann, F. F. Assaad, *SciPost Phys.* **3**, 013 (2017).
15. ALF Collaboration, *et al.*, *arXiv:2012.11914* (2021).

16. D. Bohm, D. Pines, *Phys. Rev.* **92**, 609 (1953).
17. E. H. Hwang, S. Das Sarma, *Phys. Rev. B* **75**, 205418 (2007).
18. S. Das Sarma, E. H. Hwang, W.-K. Tse, *Phys. Rev. B* **75**, 121406 (2007).
19. J. González, F. Guinea, M. A. H. Vozmediano, *Phys. Rev. B* **59**, R2474 (1999).
20. D. T. Son, *Phys. Rev. B* **75**, 235423 (2007).
21. M. E. Peskin, D. V. Schroeder, *An introduction to quantum field theory* (Westview, Boulder, CO, 1995).
22. E. G. Mishchenko, *EPL (Europhysics Letters)* **83**, 17005 (2008).
23. V. Juričić, O. Vafek, I. F. Herbut, *Phys. Rev. B* **82**, 235402 (2010).
24. J. E. Drut, D. T. Son, *Phys. Rev. B* **77**, 075115 (2008).
25. I. F. Herbut, V. Juričić, B. Roy, *Phys. Rev. B* **79**, 085116 (2009).
26. A. Giuliani, V. Mastropietro, *Phys. Rev. B* **79**, 201403 (2009).